

# Planck 2013 results. III. LFI systematic uncertainties

Planck Collaboration: N. Aghanim<sup>58</sup>, C. Armitage-Caplan<sup>89</sup>, M. Arnaud<sup>72</sup>, M. Ashdown<sup>69,6</sup>, F. Atrio-Barandela<sup>17</sup>, J. Aumont<sup>58</sup>, C. Baccigalupi<sup>83</sup>, A. J. Banday<sup>92,8</sup>, R. B. Barreiro<sup>65</sup>, E. Battaner<sup>93</sup>, K. Benabed<sup>59,91</sup>, A. Benoît<sup>56</sup>, A. Benoit-Lévy<sup>25,59,91</sup>, J.-P. Bernard<sup>8</sup>, M. Bersanelli<sup>34,48</sup>, P. Bielewicz<sup>92,8,83</sup>, J. Bobin<sup>72</sup>, J. J. Bock<sup>67,9</sup>, A. Bonaldi<sup>68</sup>, L. Bonavera<sup>65</sup>, J. R. Bond<sup>7</sup>, J. Borrill<sup>12,86</sup>, F. R. Bouchet<sup>59,91</sup>, M. Bridges<sup>69,6,62</sup>, M. Bucher<sup>1</sup>, C. Burigana<sup>47,32</sup>, R. C. Butler<sup>47</sup>, J.-F. Cardoso<sup>73,1,59</sup>, A. Catalano<sup>74,71</sup>, A. Chamballu<sup>72,14,58</sup>, L.-Y. Chiang<sup>61</sup>, P. R. Christensen<sup>80,37</sup>, S. Church<sup>88</sup>, S. Colombi<sup>59,91</sup>, L. P. L. Colombo<sup>24,67</sup>, B. P. Crill<sup>67,81</sup>, M. Cruz<sup>19</sup>, A. Curto<sup>6,65</sup>, F. Cuttaia<sup>47</sup>, L. Danese<sup>83</sup>, R. D. Davies<sup>68</sup>, R. J. Davis<sup>68</sup>, P. de Bernardis<sup>33</sup>, A. de Rosa<sup>47</sup>, G. de Zotti<sup>44,83</sup>, J. Delabrouille<sup>1</sup>, J. Dick<sup>83</sup>, C. Dickinson<sup>68</sup>, J. M. Diego<sup>65</sup>, H. Dole<sup>58,57</sup>, S. Donzelli<sup>48</sup>, O. Doré<sup>67,9</sup>, M. Douspis<sup>58</sup>, X. Dupac<sup>39</sup>, G. Efstathiou<sup>62</sup>, T. A. Enßlin<sup>77</sup>, H. K. Eriksen<sup>63</sup>, F. Finelli<sup>47,49</sup>, O. Formi<sup>92,8</sup>, M. Frailis<sup>46</sup>, E. Franceschi<sup>47</sup>, T. C. Gaier<sup>67</sup>, S. Galeotta<sup>46</sup>, K. Ganga<sup>1</sup>, M. Giard<sup>92,8</sup>, Y. Giraud-Héraud<sup>1</sup>, E. Gjerløw<sup>63</sup>, J. González-Nuevo<sup>65,83</sup>, K. M. Górski<sup>67,95</sup>, S. Gratton<sup>69,62</sup>, A. Gregorio<sup>35,46</sup>, A. Gruppuso<sup>47</sup>, F. K. Hansen<sup>63</sup>, D. Hanson<sup>78,67,7</sup>, D. Harrison<sup>62,69</sup>, S. Henrot-Versillé<sup>70</sup>, C. Hernández-Monteagudo<sup>11,77</sup>, D. Herranz<sup>65</sup>, S. R. Hildebrandt<sup>9</sup>, E. Hivon<sup>59,91</sup>, M. Hobson<sup>6</sup>, W. A. Holmes<sup>67</sup>, A. Hornstrup<sup>15</sup>, W. Hovest<sup>77</sup>, K. M. Huffmanberger<sup>94</sup>, T. R. Jaffe<sup>92,8</sup>, A. H. Jaffe<sup>54</sup>, J. Jewell<sup>67</sup>, W. C. Jones<sup>27</sup>, M. Juvela<sup>26</sup>, P. Kangaslahti<sup>67</sup>, E. Keihänen<sup>26</sup>, R. Keskitalo<sup>22,12</sup>, K. Kiiveri<sup>26,42</sup>, T. S. Kisner<sup>76</sup>, J. Knoche<sup>77</sup>, L. Knox<sup>28</sup>, M. Kunz<sup>16,58,3</sup>, H. Kurki-Suonio<sup>26,42</sup>, G. Lagache<sup>58</sup>, A. Lähteenmäki<sup>2,42</sup>, J.-M. Lamarre<sup>71</sup>, A. Lasenby<sup>6,69</sup>, R. J. Laureijs<sup>40</sup>, C. R. Lawrence<sup>67</sup>, J. P. Leahy<sup>68</sup>, R. Leonardi<sup>39</sup>, J. Lesgourgues<sup>90,82</sup>, M. Liguori<sup>31</sup>, P. B. Lilje<sup>63</sup>, V. Lindholm<sup>26,42</sup>, M. Linden-Vørnle<sup>15</sup>, M. López-Caniego<sup>65</sup>, P. M. Lubin<sup>29</sup>, J. F. Macías-Pérez<sup>74</sup>, D. Maino<sup>34,48</sup>, N. Mandolesi<sup>47,5,32</sup>, M. Maris<sup>46</sup>, D. J. Marshall<sup>72</sup>, P. G. Martin<sup>7</sup>, E. Martínez-González<sup>65</sup>, S. Masi<sup>33</sup>, S. Matarrese<sup>31</sup>, F. Matthai<sup>77</sup>, P. Mazzotta<sup>36</sup>, P. R. Meinhold<sup>29</sup>, A. Melchiorri<sup>33,50</sup>, L. Mendes<sup>39</sup>, A. Mennella<sup>34,48</sup>, M. Migliaccio<sup>62,69</sup>, S. Mitra<sup>53,67</sup>, A. Moneti<sup>59</sup>, L. Montier<sup>92,8</sup>, G. Morgante<sup>47</sup>, D. Mortlock<sup>54</sup>, A. Moss<sup>85</sup>, D. Munshi<sup>84</sup>, P. Naselsky<sup>80,37</sup>, P. Natoli<sup>32,4,47</sup>, C. B. Netterfield<sup>20</sup>, H. U. Nørgaard-Nielsen<sup>15</sup>, D. Novikov<sup>54</sup>, I. Novikov<sup>80</sup>, I. J. O'Dwyer<sup>67</sup>, S. Osborne<sup>88</sup>, F. Paci<sup>83</sup>, L. Pagano<sup>33,50</sup>, R. Paladini<sup>55</sup>, D. Paoletti<sup>47,49</sup>, B. Partridge<sup>41</sup>, F. Pasian<sup>46</sup>, G. Patanchon<sup>1</sup>, D. Pearson<sup>67</sup>, M. Peel<sup>68</sup>, O. Perdereau<sup>70</sup>, L. Perotto<sup>74</sup>, F. Perrotta<sup>83</sup>, E. Pierpaoli<sup>24</sup>, D. Pietrobon<sup>67</sup>, S. Plaszczynski<sup>70</sup>, P. Platania<sup>66</sup>, E. Pointecouteau<sup>92,8</sup>, G. Polenta<sup>4,45</sup>, N. Ponthieu<sup>58,51</sup>, L. Popa<sup>60</sup>, T. Poutanen<sup>42,26,2</sup>, G. W. Pratt<sup>72</sup>, G. Prézeau<sup>9,67</sup>, S. Prunet<sup>59,91</sup>, J.-L. Puget<sup>58</sup>, J. P. Rachen<sup>21,77</sup>, R. Rebolo<sup>64,13,38</sup>, M. Reinecke<sup>77</sup>, M. Remazeilles<sup>58,1</sup>, S. Ricciardi<sup>47</sup>, T. Riller<sup>77</sup>, G. Rocha<sup>67,9</sup>, C. Rosset<sup>1</sup>, M. Rossetti<sup>34,48</sup>, G. Roudier<sup>1,71,67</sup>, J. A. Rubiño-Martín<sup>64,38</sup>, B. Rusholme<sup>55</sup>, M. Sandri<sup>47</sup>, D. Santos<sup>74</sup>, D. Scott<sup>23</sup>, M. D. Seiffert<sup>67,9</sup>, E. P. S. Shellard<sup>10</sup>, L. D. Spencer<sup>84</sup>, J.-L. Starck<sup>72</sup>, V. Stolyarov<sup>6,69,87</sup>, R. Stompor<sup>1</sup>, F. Sureau<sup>72</sup>, D. Sutton<sup>62,69</sup>, A.-S. Suur-Uski<sup>26,42</sup>, J.-F. Sygnet<sup>59</sup>, J. A. Tauber<sup>40</sup>, D. Tavagnacco<sup>46,35</sup>, L. Terenzi<sup>47</sup>, L. Toffolatti<sup>18,65</sup>, M. Tomasi<sup>48</sup>, M. Tristram<sup>70</sup>, M. Tucci<sup>16,70</sup>, J. Tuovinen<sup>79</sup>, M. Türlér<sup>52</sup>, G. Umana<sup>43</sup>, L. Valenziano<sup>47</sup>, J. Valiviita<sup>42,26,63</sup>, B. Van Tent<sup>75</sup>, J. Varis<sup>79</sup>, P. Vielva<sup>65</sup>, F. Villa<sup>47</sup>, N. Vittorio<sup>36</sup>, L. A. Wade<sup>67</sup>, B. D. Wandelt<sup>59,91,30</sup>, R. Watson<sup>68</sup>, A. Wilkinson<sup>68</sup>, D. Yvon<sup>14</sup>, A. Zacchei<sup>46</sup>, and A. Zonca<sup>29</sup>

(Affiliations can be found after the references)

Preprint online version: March 27, 2013

## ABSTRACT

We present the current estimate of instrumental and systematic effect uncertainties for the *Planck*-Low Frequency Instrument relevant to the first release of the *Planck* cosmological results. We discuss an overview of the main effects and of the tools and methods applied to assess the residuals on maps and power spectra. We also present an overall budget of systematic effect uncertainties, which are dominated by far sidelobe straylight pick-up and imperfect calibration. They are at least two orders of magnitude less than the cosmic microwave background (CMB) temperature power spectrum. A residual spurious signal above the noise level is present, especially at 30 GHz, in the multipole range  $\ell < 20$ , and is likely to be caused by residual Galactic straylight contamination. Current analysis aims to further reduce the level of spurious signals in the data and to better model systematic effects, in particular straylight and calibration uncertainties.

**Key words.** cosmology: cosmic background radiation; cosmology: observations; methods: data analysis

## Contents

<b>1</b>	<b>Introduction</b>	<b>2</b>	3.2	Effects dependent on sky signal . . . . .	7
<b>2</b>	<b>Summary of uncertainties due to systematic effects</b>	<b>2</b>	3.2.1	Sidelobe pick-up . . . . .	7
<b>3</b>	<b>Overview of LFI systematic effects</b>	<b>3</b>	3.2.2	ADC non linearity . . . . .	7
3.1	Effects independent of sky signal . . . . .	5	3.2.3	Imperfect photometric calibration . . . . .	8
3.1.1	Noise correlations and $1/f$ noise . . . . .	5	3.3	Pointing effects . . . . .	8
3.1.2	Thermal effects . . . . .	5	<b>4</b>	<b>Assessing residual systematic effect uncertainties in maps and power spectra</b>	<b>9</b>
3.1.3	Bias fluctuations . . . . .	6	4.1	Null tests . . . . .	9
3.1.4	1-Hz spikes . . . . .	7	4.1.1	Half-ring difference null tests . . . . .	9
			4.1.2	Survey difference null tests . . . . .	9
			4.2	Assessment of timeline-additive systematic effects	11
			4.2.1	Thermal effects . . . . .	11
			4.2.2	Bias fluctuations . . . . .	13
			4.2.3	1-Hz spikes . . . . .	13

\* Corresponding author: A. Mennella [aniello.mennella@fisica.unimi.it](mailto:aniello.mennella@fisica.unimi.it)

4.3	Assessment of effects dependent on the sky . . .	13
4.3.1	Sidelobes . . . . .	13
4.3.2	ADC non-linearity . . . . .	15
4.3.3	Imperfect photometric calibration . . . .	16
4.4	Pointing uncertainties . . . . .	16
4.5	Propagation of systematic uncertainties in component separation . . . . .	17
4.6	Gaussianity statistical tests . . . . .	18
5	Conclusions	18
A	Theory of the ADC non-linearity effect	20

## 1. Introduction

This paper, one of a set associated with the 2013 release of data from the *Planck*<sup>1</sup> mission (Planck Collaboration I 2013), describes the *Planck*-LFI instrument systematic effects and their related uncertainties in CMB temperature maps and power spectra.

The LFI implements a pseudo-correlation differential design similar to *WMAP* (Jarosik et al. 2003; Jarosik et al. 2003) to suppress  $1/f$  amplifier gain and noise fluctuations (Seiffert et al. 2002; Mennella et al. 2003; Bersanelli et al. 2010) as well as correlated effects from thermal and electrical variations affecting both the sky signal and reference loads. The reference signal is provided by stable 4.5 K blackbodies thermally and mechanically connected to the external structure of the High Frequency Instrument (HFI) 4 K box (Valenziano et al. 2009; Lamarre et al. 2010). The offset between the sky and reference signals, of the order of 1–2 K, is balanced in software during data processing on the ground (Mennella et al. 2003; Zacchei et al. 2011). The differenced timestreams are characterised by  $1/f$  noise knee frequencies in the range 10–100 mHz (Mennella et al. 2010, 2011), leaving residual correlated low-frequency fluctuations in gain and signal that are removed during calibration and map-making.

The LFI is also an excellent polarimeter, with very low systematic effects. Depolarization by the optics and by imperfections in the orthomode transducers, separating the orthogonal linear polarizations, has been accurately measured on the ground and is almost negligible (Leahy et al. 2010).

Asymmetrical bandpass response in the two radiometers is the main source of  $I \rightarrow (Q, U)$  leakage in the foreground-dominated sky regions, especially at low frequencies. Although accurate knowledge of the bandpass response allows us, in principle, correction for this effect during data analysis, the ground bandpass measurements were not accurate enough to maintain this residual below 1% (Zonca et al. 2009). For this reason the spurious polarization from bandpass mismatch was estimated and removed using flight data, as described in Planck Collaboration II (2013).

Optical effects arise mainly from Galactic and CMB dipole pick-up caused by primary and secondary mirror spillovers (Tauber et al. 2010; Sandri et al. 2010). This is relevant especially for polarization measurements at 30 GHz, where Galactic emissions are stronger.

In this paper we provide a comprehensive overview of the instrument systematic effects and the uncertainties they cause

on CMB temperature maps and power spectra (see Sect. 2). In Sect. 3 we outline and discuss the known instrumental effects, separating them into two broad categories: (i) effects that do not depend on the sky signal and impact the radiometric measurements as an additive spurious fluctuation or a gain variation, and (ii) effects that depend on the sky signal, i.e., on its amplitude and/or on the scanned sky region. Some of these effects are removed in the data processing pipeline according to algorithms described in Planck Collaboration II (2013). The assessment of the residual uncertainty, discussed in Sect. 4, was performed according to two different strategies. Null tests were the primary tool to check for systematic effect residuals exceeding the white noise level. We also assessed their impact on radiometric timelines, even if below the white noise limit, by exploiting in-flight housekeeping and scientific data. This latter approach, that combines flight data with ground-measured instrument properties, has never been applied in previous CMB experiments and proved a powerful tool to check for systematic effects.

Some of the effects discussed in this paper are also relevant for calibration, and are discussed in detail in Planck Collaboration V (2013). In this case we provide here only a brief discussion of the most relevant points and results, deferring to the dedicated paper any further details.

Throughout this paper we follow the naming convention described in Appendix A of Mennella et al. (2010) and also available on-line on the Explanatory Supplement (Planck Collaboration ES 2013).

## 2. Summary of uncertainties due to systematic effects

In this section we provide a top-level overview of the uncertainties due to systematic effects in the *Planck*-LFI CMB temperature maps and power spectra. Table 1 provides a list of these effects, with short descriptions of their cause, strategies for their removal and references to sections and/or papers where more information can be found.

The impact of  $1/f$  noise has been assessed using “half-ring” noise maps (see Sect. 4.1.1) normalized to the white noise estimate at each pixel obtained from the white noise covariance matrix, so that a perfectly white noise map would be Gaussian and isotropic with unit variance. Deviations from unity trace the contribution of residual  $1/f$  noise in the final maps, which ranges from 0.06% at 70 GHz to 2% at 30 GHz, as detailed in Sect. 12.2 of Planck Collaboration II (2013).

Pixel uncertainties due to other systematic effects have been calculated on simulated maps degraded to  $N_{\text{side}} = 128$  at 30 and 44 GHz and  $N_{\text{side}} = 256$  at 70 GHz in order to approximate the optical beam size.

In Table 2 we list the r.m.s. and the difference between the 99% and the 1% quantiles in the pixel value distributions. For simplicity we refer to this difference as the peak-to-peak (p-p) difference, although it neglects outliers but effectively approximates the peak-to-peak variation of the effect on the map.

The last row in Table 2 reports the r.m.s. value of survey difference maps (first minus second survey), after a correction which takes into account the white noise (see Sect. 4.1.2 for details about this correction). These values thus represent the level of r.m.s. uncertainty per pixel due to known and unknown systematic effects.

Angular power spectra have been obtained from full resolution ( $N_{\text{side}} = 1024$ ) systematic effect maps at each frequency using the HEALPix Anafast routine (Górski et al. 2005). We

<sup>1</sup> *Planck* (<http://www.esa.int/Planck>) is a project of the European Space Agency (ESA) with instruments provided by two scientific consortia funded by ESA member states (in particular the lead countries France and Italy), with contributions from NASA (USA) and telescope reflectors provided by a collaboration between ESA and a scientific consortium led and funded by Denmark.

**Table 1.** List of known instrumental systematic effects in *Planck*-LFI

Effect	Source	Control/Removal	Reference
<b>Effects independent of sky signal</b>			
White noise correlation . . . .	Phase switch imbalance . . . . .	Diode weighing . . . . .	3.1.1
1/f noise . . . . .	RF amplifiers . . . . .	Pseudo-correlation and destriping . . . .	3.1.1
Bias fluctuations . . . . .	RF amplifiers, back-end electronics	Pseudo-correlation and destriping . . . .	3.1.3
Thermal fluctuations . . . . .	4 K, 20 K and 300 K thermal stages	Calibration, destriping . . . . .	3.1.2, 4.2.1
1 Hz spikes . . . . .	Back-end electronics . . . . .	Template fitting and removal . . . . .	3.1.4, 4.2.3
<b>Effects dependent on the sky signal</b>			
Sidelobe pickup . . . . .	Main and sub-reflector spillovers .	Model sidelobes removed from timelines (not implemented in this release)	3.2.1, 4.3.1
Bandpass asymmetries . . . .	Differential orthomode transducer and receiver bandpass response	Spurious polarisation removal . . . . .	Planck Collaboration II (2013)
Analogue-to-digital converter non linearity	Back-end analogue-to-digital . . . converter	Template fitting and removal . . . . .	3.2.2, 4.3.2 Planck Collaboration II (2013)
Imperfect photometric calibration	Sidelobe pickup, radiometer noise temperature changes and other non-idealities	Calibration using the 4 K reference . . . load voltage output	3.2.3, 4.3.3, Planck Collaboration V (2013)
Pointing . . . . .	Uncertainties in pointing reconstruction, thermal changes affecting focal plane geometry	Negligible impact on temperature . . . . anisotropy measurements	3.3, 4.4

**Table 2.** Summary of systematic effects uncertainties on maps<sup>a</sup> in  $\mu\text{K}_{\text{CMB}}$ .

	30 GHz		44 GHz		70 GHz	
	p-p	rms	p-p	rms	p-p	rms
Bias fluctuations . . . . .	0.08	0.01	0.10	0.02	0.23	0.06
Thermal fluctuations . . .	0.61	0.11	0.40	0.08	1.17	0.20
1-Hz spikes . . . . .	0.87	0.17	0.14	0.03	0.60	0.12
Sidelobes pickup . . . . .	18.95	4.53	1.92	0.57	6.39	1.91
ADC non-linearity . . . .	3.87	1.01	0.89	0.19	0.92	0.19
Gain residuals . . . . .	4.33	1.16	4.74	0.97	6.51	1.10
Total <sup>b</sup> . . . . .	21.02	4.83	5.61	1.13	7.87	2.00
Survey consistency <sup>c</sup> . . . . .	8.50	...	7.10	...	8.20	...

<sup>a</sup> Calculated on a pixel size approximately equal to the average beam FWHM.

<sup>b</sup> The total has been computed on maps resulting from the sum of individual systematic effect maps.

<sup>c</sup> Measured r.m.s. of the half-difference between two complete sky surveys minus the r.m.s. of the noise for pixels, see Sect. 4.1.2.

have then evaluated the propagation of the various effects in the final CMB map by assuming a simple internal linear combination component separation, as explained in Sect. 4.5. In Fig. 1 we show how the power spectra of the various effects compare with the *Planck* temperature spectrum, with the noise level coming from the half-ring difference maps (see Sect. 4.1.1) and with the residual map obtained from a difference map between survey

1 and survey 2<sup>2</sup> (see Sect. 4.1.2). The large plot in the top panel shows the power spectra obtained from frequency-independent maps resulting from the weighted-average of frequency maps using the weights specified in Sect. 4.5. Spectra in the three small plots in the lower panel, instead, show contributions of systematic effects from individual frequency maps.

Our assessment shows that the global impact of systematic effect uncertainties is at least two order of magnitudes less than the CMB power spectrum, and demonstrates the robustness of *Planck*-LFI temperature anisotropy measurements. Comparison between the total simulated systematic effects and residual signal obtained by differencing survey 1 and survey 2 maps highlights an excess signal in the multipole range  $\ell \lesssim 20$  that is not completely accounted for in our simulations. This excess comes mainly from the 30 GHz channel and is likely to be caused by Galactic emissions picked up by beam sidelobes. Understanding this excess and further reducing the level of residual systematic uncertainties is the primary goal of our current analysis to obtain polarization measurements with a level of purity comparable to what has been achieved for temperature anisotropies.

### 3. Overview of LFI systematic effects

Known systematic effects in the *Planck*-LFI data can be divided into two broad categories: effects independent of the sky signal, which can be considered as additive or multiplicative spurious contributions to the measured timelines, and effects which are dependent on the sky and that cannot be considered independently of the observational strategy.

<sup>2</sup> Time periods relative to individual surveys are defined in Table 11 of Planck Collaboration II (2013)

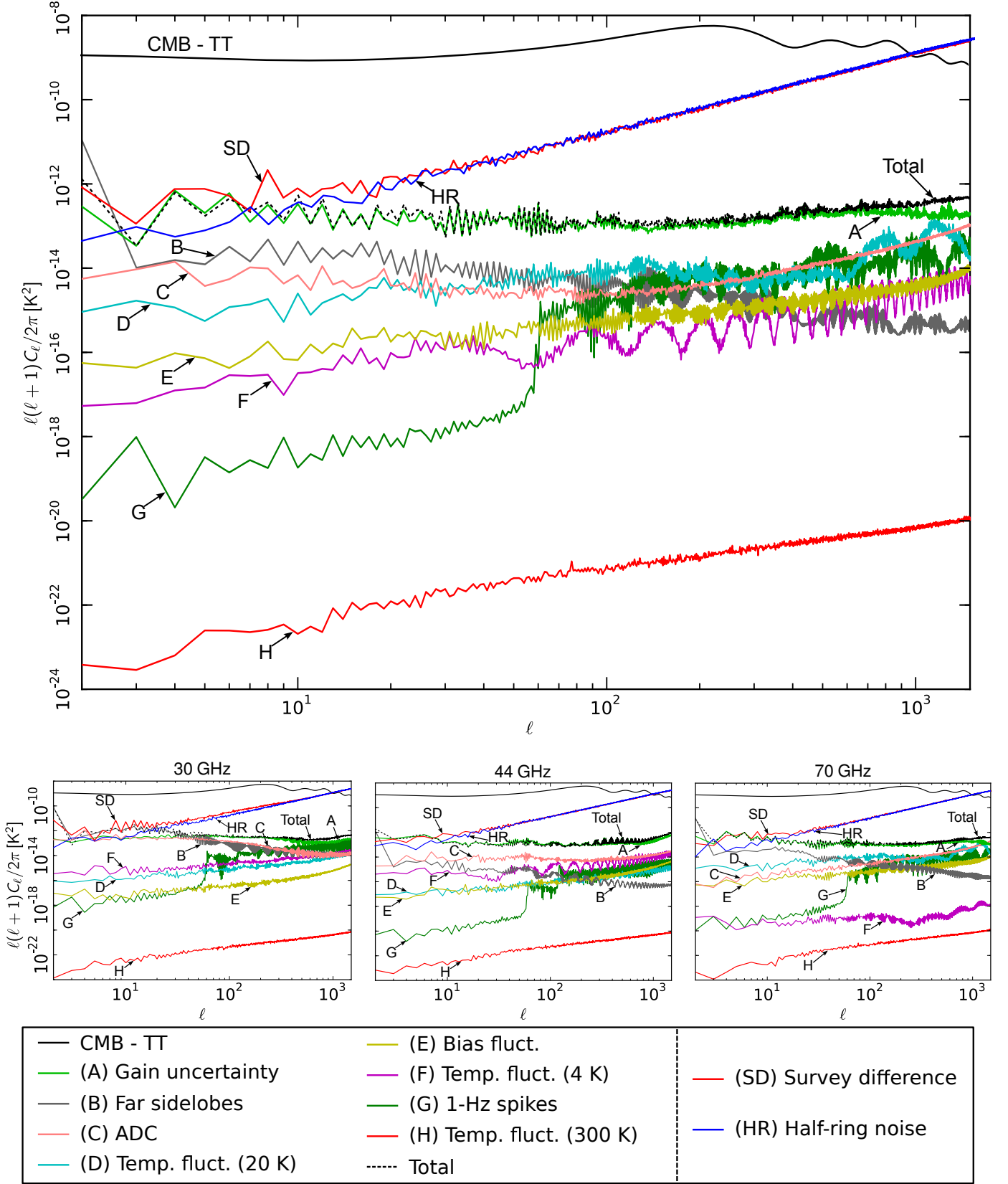


**Fig. 1.** Angular power spectra of the various systematic effects compared to the *Planck* temperature anisotropy spectrum. The black dashed curve, representing the total contribution, has been derived from a map where all the systematic effects have been summed. *Top panel:* power spectra obtained from frequency independent maps resulting from the weighted-average of individual systematic effect frequency maps. *Bottom panel:* contributions of systematic effects from individual frequency maps. The CMB curve corresponds to the *Planck* best-fit model presented in [Planck Collaboration XV \(2013\)](#).



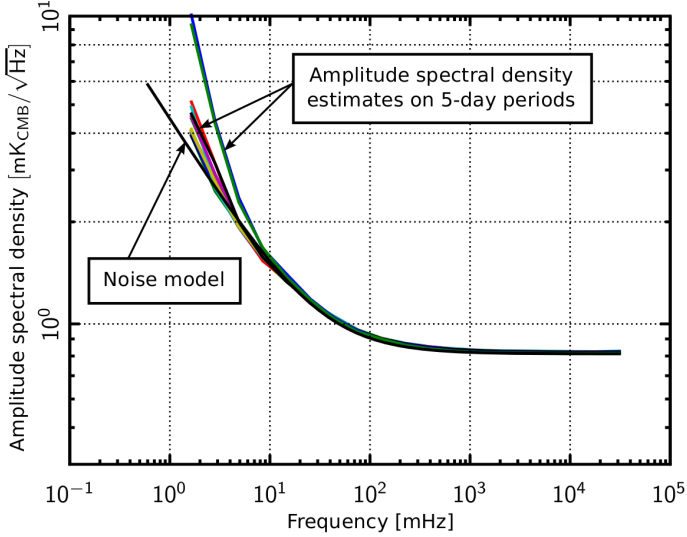


**Fig. 2.** Amplitude spectral density estimates on 5-day time periods (coloured lines) compared to the nominal mission noise model for a representative 70 GHz radiometer (LFI23M).

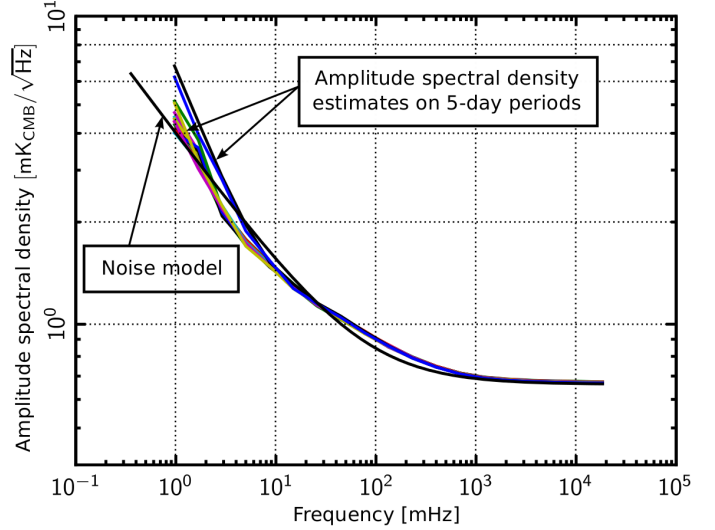


**Fig. 3.** Amplitude spectral density estimates on 5-day time periods (coloured lines) compared with the nominal mission noise model (black line) for one 44 GHz radiometer (LFI24S).

### 3.1. Effects independent of sky signal

#### 3.1.1. Noise correlations and $1/f$ noise

Each *Planck*-LFI receiver is a pseudo-correlation system viewing a scalar feed directed through the telescope at the sky, together with a reference cold load thermally stable near 4 K. Non-white noise from the cold front-end amplifiers is reduced via the correlation, while fluctuations in the later stages of the receiver are minimized by modulating a phase switch in the correlation section at 8192 Hz. The LFI receiver design, construction, ground performance and initial flight performance have been extensively documented (Bersanelli et al. 2010; Mennella et al. 2010, 2011).

The noise properties of the receivers play an important role in downstream data analysis. In particular, we need good estimates of the white noise level, long term stability ( $1/f$ -type noise) and any correlated noise components.

The receiver architecture is symmetric, with two complementary detector diodes as output for each receiver channel. As described in Seiffert et al. (2002) and Mennella et al. (2011) imperfect matching of components generates isolation between the complementary diodes of a receiver between  $-10$  and  $-15$  dB. This imperfect isolation leads to a small anti-correlated component in the white noise that is cancelled by a weighted average of the time ordered data from the two diodes of each receiver as the first step of analysis. This avoids the complication of tracking the anti correlated white noise throughout the analysis.

We treat the combined diode data as the raw data, and calibration, noise estimation, map-making etc. are performed on these combined data. The weights were determined from some initial estimates of the calibrated noise for each detector, and are kept fixed for the entire mission.

Noise parameters were reported in Mennella et al. (2011). A longer data set, some thermal instabilities in the instrument (particularly during survey 3), and refinements of the data analysis (map making and noise covariance matrix) all require a more detailed look at the long term evolution of the noise characteristics of the receivers.

The noise power spectral density  $P(f)$  of the receivers is generally well described by

$$P(f) = \sigma^2 \left[ 1 + \left( \frac{f}{f_k} \right)^\alpha \right], \quad (1)$$

where  $\sigma$  characterizes the white noise component, the knee frequency,  $f_k$ , denotes the frequency where white noise and  $1/f$  contribute equally in power to the total noise, and  $\alpha$  characterizes the slope of the power spectrum for frequencies  $f < f_k$ .

We estimate the signal-subtracted noise power spectrum of each receiver on 5-day time periods. Except for specific, mostly well understood events, shorter time scale noise estimation does not produce any evident trends. For nearly all the radiometers our noise model is a very good approximation of the power spectrum. We plot a representative comparison in Fig. 2. A few channels show features not well captured by this simple model; the worst is displayed in Fig. 3.

Over the course of the nominal mission, the noise is well fit by the model, with the exception of the early parts of sky survey 3. During this time, thermal instabilities brought on by the switch-over from the nominal to the redundant sorption cooler cause poor fits and some changes in the parameters. In Figs. 4 through 6 we show the behaviour of the three noise parameters in Eq. (1) estimated on 5-day sections of data over the nominal time period. White noise and knee frequency are stable, while the slope starts increasing in absolute value after day 300, as a result of larger temperature fluctuations in the 20 K focal plane. The jump in slope after day 500 is correlated with the sorption cooler switch-over (see Sect. 3.1.2 for further details).

#### 3.1.2. Thermal effects

The LFI is susceptible to temperature fluctuations in the 300 K back-end modules, in the 4 K reference loads and in the 20 K focal plane. Figure 7 provides an overview of the main temperatures during the period between day 91 (the start of nominal operations) and 563 after launch.

The two topmost plots show the reference load temperatures at the level of the 70 GHz and 30–44 GHz channels, re-

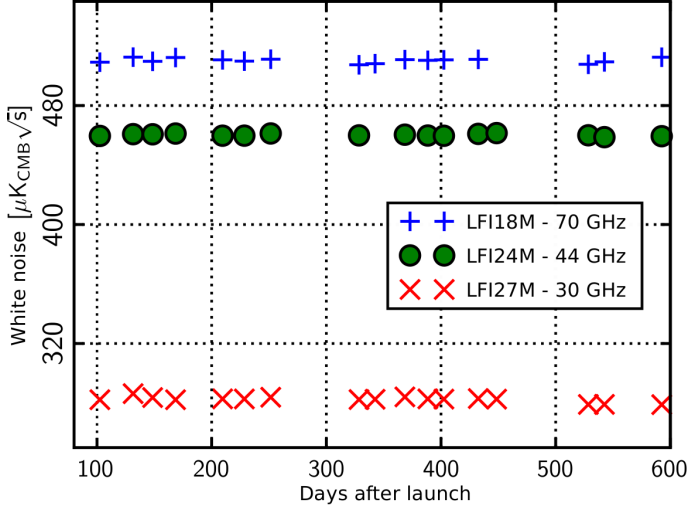


**Fig. 4.** Fitted white noise parameters over the nominal survey for representative radiometers at 30, 44 and 70 GHz. Values are estimated on 5-day sections of data.

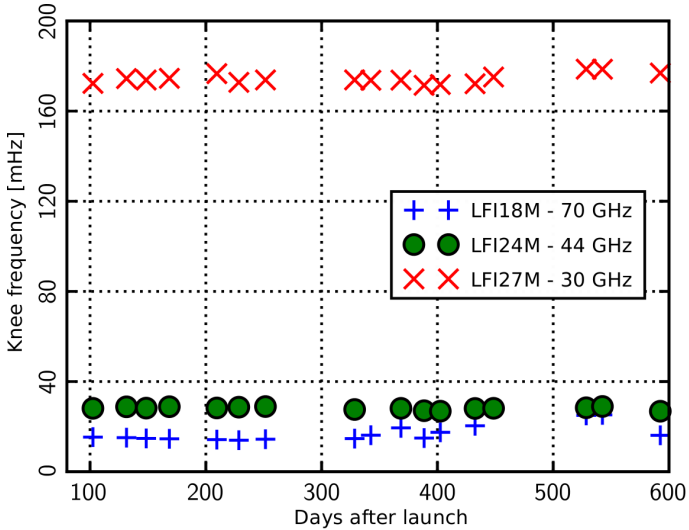


**Fig. 5.** Fitted knee frequencies over the nominal survey for representative radiometers at 30, 44 and 70 GHz. Values are estimated on 5-day sections of data.

spectively. The temperature of the 70 GHz reference loads is actively controlled by a proportional-integral-derivative (PID) system and is very stable ( $\delta T_{\text{rms}} \sim 0.13$  mK, see the zoomed plot in the inset). Reference loads of the 30 and 44 GHz channels, instead, do not benefit from active thermal control. Their temperature is consequently more unstable and susceptible to major system-level events like, for example, the switchover to the redundant sorption cooler.

The third plot from the top of Fig. 7 shows the 20 K LFI focal plane temperature measured by a sensor placed on the feed horn flange of the LFI28 receiver. The temperature during the first sky survey was very stable, with a  $\delta T_{\text{rms}} \lesssim 1$  mK. Towards the end of the first year of operations the sorption cooler performance started to degrade and its stability was maintained with a series of controlled temperature changes. The switchover to the redundant cooler was performed on August, 11<sup>th</sup> 2010, leaving a

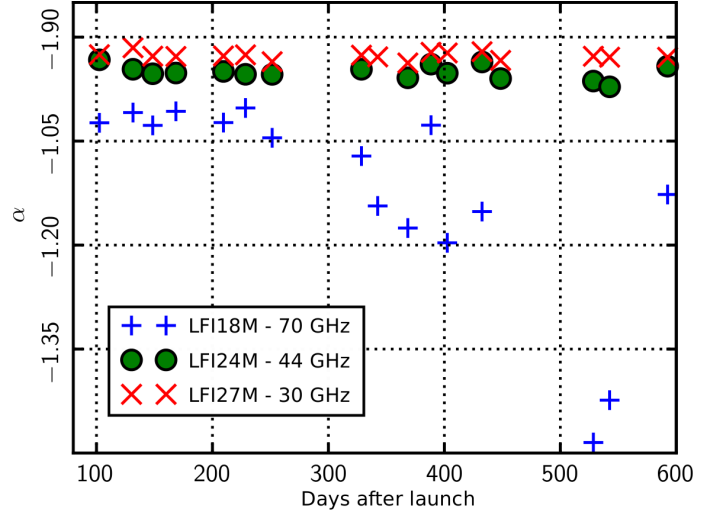


**Fig. 6.** Fitted power-law slopes for low frequency noise. Here we note significant instability during the early part of the third survey. This is due to substantially greater thermal instability of the 20 K stage just before and after switchover between the two sorption coolers.

clear signature on all the main LFI temperatures. After this operation the level of temperature fluctuations in the focal plane increased unexpectedly, and this was later understood to be the effect of liquid hydrogen that was still present in the cold-end of the nominal cooler, because the degraded compressor system was not able to absorb all the hydrogen that was present in the cooler line. Although this effect was later mitigated by a series of dedicated operations, most of the third sky survey suffered from a higher-than-nominal level of temperature variation.

The last plot shows the temperature of the 300 K electronics box, measured by one of its temperature sensors. During the first sky survey the back-end temperature suffered from a daily fluctuation caused by the satellite transponder that was switched on daily during contact with the ground station. After day 258 the system was left continuously on, and the modulation disappeared. This operation caused an increase of the absolute temperature level. The second temperature change occurred in correspondence to the sorption cooler switch-over operation. The plot also shows a yearly temperature modulation due to the satellite rotation around the Sun and a temperature spike at day 191 after launch. This was caused by an operational anomaly that led the satellite to fail to repoint for an entire day with a corresponding temperature increase of the warm units.

More details about the thermal stability performance of *Planck* can be found in [Planck Collaboration II \(2011\)](#), while the susceptibility of the LFI to temperature variations is discussed in [Terenzi et al. \(2009\)](#).

### 3.1.3. Bias fluctuations

The signal detected by the radiometers can vary because of fluctuations in the front-end and back-end amplifier bias voltages. In the LFI these fluctuations occurred according to two time scales:

- slow electric drifts, due to thermal changes in the power supply, in the RF amplifiers, and in the detector diodes;
- fast and sudden electric instabilities, arising in the warm electronics or from electromagnetic interference effects, and

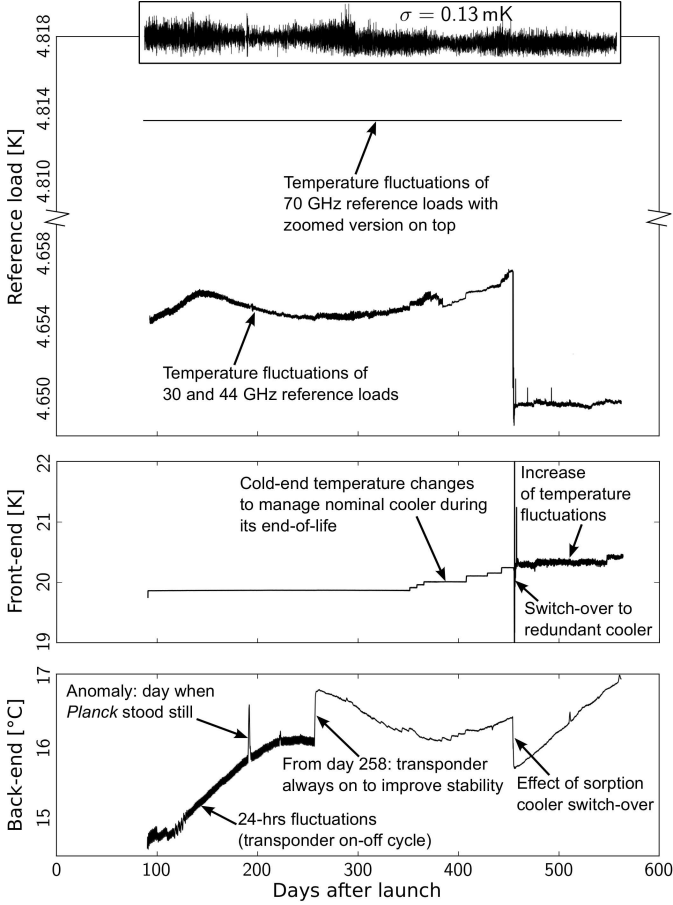


**Fig. 7.** Main temperatures in *Planck*-LFI. From top to bottom: 70 GHz reference loads, 30 and 44 GHz reference loads, 20 K focal plane (sensor placed on feed horn flange of LFI28) and 300 K back-end (sensor placed on the back-end electronics box). A brief description of the main operational events affecting the thermal behaviour is provided in each panel.

affecting both the cold amplifiers and the warm detector diodes.

The effect of slow drifts is suppressed by the pseudo-correlation architecture of the differential radiometers. Fast electric changes produce quasi-random fluctuations and abrupt steep drops or jumps in the signal. If jumps are caused by instabilities in the front-end bias voltage then the effect involves the output voltage of both diodes in the radiometer. When the jumps occur in the back-end detector diodes (so-called “popcorn noise”) they impact only the output voltage of the corresponding diode and affect sky and reference load samples. In both cases the differenced signal is largely immune from these effects.

#### 3.1.4. 1-Hz spikes

This effect is caused by pickup from the housekeeping electronics clock that occurs after the detector diodes and before the analogue-to-digital converter (ADC) (Meinhold et al. 2009; Mennella et al. 2010, 2011). This spurious signal is detected in the radiometer time-domain outputs as a 1 s square wave with a rising edge near 0.5 s and a falling edge near 0.75 s in on-board time. In the frequency domain it appears at multiples of 1 Hz.

Frequency spikes are present at some level in the output from all detectors, but affect the 44 GHz data most strongly because

of the low voltage output and high post-detection gain values in that channel. For this reason spikes are removed from the 44 GHz time-ordered data via template fitting, as described in Planck Collaboration II (2013).

### 3.2. Effects dependent on sky signal

#### 3.2.1. Sidelobe pick-up

Straylight contamination arises from the spurious signal pickup from the telescope far sidelobes. Main sources of straylight contamination are the Galaxy, especially at 30 GHz, and the cosmological dipole, mainly detected in the directions of the main and sub-reflector spillover, as sketched in Fig. 8. In principle we should also include the straylight contribution from the orbital dipole, but its effect is a factor ten lower than the cosmic dipole, so that it can safely be neglected in this framework (but it has been considered in the calibration pipeline). Further details about the *Planck* optical system are reported in Tauber et al. (2010), while the LFI beam properties are provided in Sandri et al. (2010).

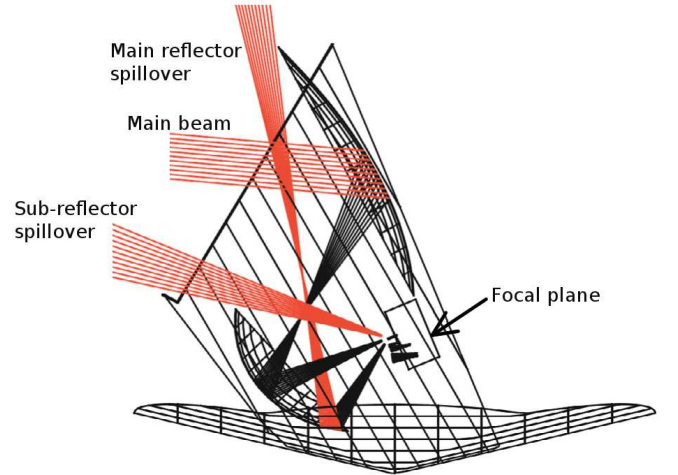


**Fig. 8.** Main and sub-reflector spillover, and main beam directions in the *Planck* telescope.

Straylight impacts the measured signal in two ways: (i) through direct contamination and coupling with the main beam sky signal, and (ii) in the photometric calibration of the radiometer detected signal. In this paper we concentrate on the direct detection, while the impact on calibration and the adopted mitigation strategies are described in Planck Collaboration V (2013).

Because of the beam orientation, the straylight fingerprint is different in odd surveys compared to even surveys. The Galaxy, for example, is detected by the sub-reflector spillover in the odd surveys and by the main-reflector spillover in the even surveys. Because the sub-reflector spillover points approximately in the main beam direction, the Galaxy straylight pattern is close to the Galactic plane. The main-reflector spillover, instead, points at about  $85^\circ$  from the main beam so that the Galaxy is re-imaged onto a ring (see figures in Sect. 4.3.1).

#### 3.2.2. ADC non linearity

The ADC linearity requires that the voltage step sizes between successive binary outputs are constant over the entire input dynamic range. If these steps are not constant (see the sketch in

Fig. 9) we have a non linearity in the ADC response that leads to calibration errors. A brief description of the mathematical model of this effect is provided in Appendix A.

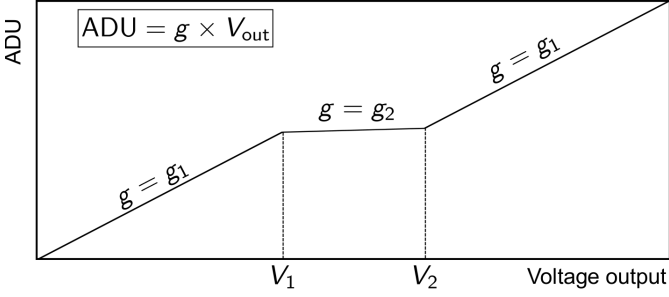


**Fig. 9.** Schematic of the ADC non-linearity effect. For a small range of voltages the ADC response changes slope.

The typical fingerprint of ADC non-linearity is a variation of the detector voltage output white noise not paired by a detectable variation in the voltage level. This effect was observed in the LFI radiometer data for the first time in flight, where drops of a few percent were observed in the voltage white noise but not in the output level over periods of few weeks. Fig. 10 shows this effect as a plot of relative white noise variation versus the detector output voltage for one of the most affected radiometer channels (the 44 GHz detector LFI25M-01).

The grey points represent an average over each pointing (about 40 min) while the solid line has been obtained by further binning the data in 200 bins over the plotted range in order to reduce the scatter and show more detail. The figure shows that the typical amplitude of the region where the non-linearity occurs is of the order of 1 mV, corresponding to about three bits in the ADC. The ADC effect is strongest (3 to 6%) in the 44 GHz channels, because of their lower detector voltages.

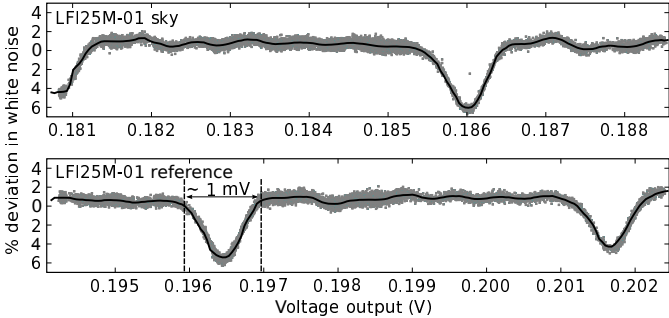


**Fig. 10.** Plots of the percentage variation in the single detector white noise estimates with detector voltage.

The ADC non-linearity effect has been characterised from flight data and removed from the data streams according to the procedure described in Planck Collaboration II (2013). In Fig. 11 we show the same data as in Fig. 10 after the correction has been applied. The figure clearly shows that the anomalous white noise dips disappear after correction.

### 3.2.3. Imperfect photometric calibration

An important set of systematic effects are those related to the photometric calibration of the radiometers. Such effects are dis-

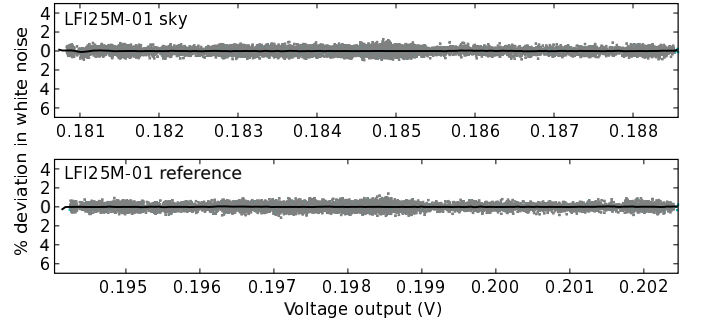


**Fig. 11.** Same as in Fig. 10 after correction of the ADC non-linearity effect.

cussed in Planck Collaboration V (2013); here we will only provide the most important information to put the results of that paper within the context of this work.

There are three different kinds of systematic effects that can affect the calibration.

1. *Incorrect assumptions regarding the calibration signal.* In the case of LFI, the signal used for the calibration is the dipolar field caused by the motion of the Solar System with respect to the CMB rest frame and by the motion of the spacecraft around the Sun. We model the former using the values quoted by Hinshaw et al. (2009) and the latter using the spacecraft's attitude information. Any error in the numbers would directly lead to an error in the calibration of Planck-LFI data.
2. *Incorrect treatment of the calibration signal.* To actually use any previous knowledge of the CMB dipole, we need to convolve the signal with the beam response of the LFI radiometers. Any error in this step would produce a systematic effect in the map, not only because of the wrong shape expected for the calibration signal, but also because of the removal of the (wrong) dipole from the calibrated maps done by the Planck-LFI pipeline (Planck Collaboration II 2013). Possible types of errors include: systematic errors in WMAP dipole estimate, wrong convolution of the expected dipole with the radiometer beams, incorrect masking of the Galaxy when fitting the observed signal with the dipole, etc.
3. *Incorrect reconstruction of gain fluctuations.* Some of the algorithms we used in calibrating LFI data for this release use the radiometer equation and the recorded variations of the radiometers total-power output to track gain changes. In principle, any deviation in the behaviour of the radiometer from the ideal case (e.g., ADC non-linearities) can induce systematic effects in the gain curves.

### 3.3. Pointing effects

Pointing uncertainties are translated into uncertainties in pixel temperature measurements. If pointing uncertainties are not constant in time then the statistics of the sky anisotropy measurements is not preserved, with a consequent impact on power spectrum and cosmological parameters. For Planck-LFI, pointing uncertainties arise from two main effects:

1. *Satellite pointing determination.* The Planck Attitude Control Movement System guarantees a pointing accuracy of about 2'' (Planck Collaboration I 2013; Planck Science Office 2010), which is well within scientific requirements. However, small non-idealities in the system and errors in



the attitude reconstruction (caused, for example, by thermo-elastic effects) can affect the data.

2. *Uncertainties in the focal plane geometry reconstruction.* The measurement of the *Planck*-LFI focal plane geometry is based on the determination of the beam pointing with respect to the nominal line of sight exploiting Jupiter observations. The peak of each beam has been determined by fitting data with a bivariate Gaussian function which may not be representative of the real beam centre.

#### 4. Assessing residual systematic effect uncertainties in maps and power spectra

In this section we discuss the assessment of the impact of residual systematic effects on maps and power spectra. This assessment has been performed according to two strategies: by “null maps” obtained by differencing maps with the same sky signal, in order to highlight residuals, and by simulating the systematic effects in the timelines, exploiting a combination of flight data and measured instrumental properties.

##### 4.1. Null tests

We define a “null test” as any difference between two independent data sets which are anticipated to give nearly the same signal, on the assumption of perfect calibration, pointing reconstruction, and systematic effects removal. Null tests are a powerful means to assess the validity and self-consistency of *Planck* data on various timescales and across different dimensions (detector, frequency, time), and to highlight systematic effects above the white noise level.

The design of *Planck* and its observing strategy provides a wide range of opportunities for null tests, with sensitivity to different systematic effects and implications for the scientific outputs. Although we refer to these tests as null tests, the results are generally not featureless, and are required to match our instrument model, in terms of far sidelobe contribution, main lobe ellipticity and orientation, and especially our noise model, captured in the noise covariance matrix produced with each map.

In the *Planck*-LFI collaboration each internal data release is accompanied by a comprehensive set of null tests as a check of our processes and ongoing improvement in terms of systematic errors. In this section we report the results from the main tests supporting the systematic effect analysis for the first *Planck* public data release.

Here we provide some sample difference maps. Unless otherwise noted, these maps are masked to remove point sources and to include only pixels measured in both maps. Difference maps are divided by 2 to be statistically consistent with average maps, and are smoothed to  $2^\circ$  FWHM to enhance large scale features.

##### 4.1.1. Half-ring difference null tests

Half-ring difference null tests, constructed by taking a weighted difference between the first and second halves of each pointing period, are useful to assess the data noise properties and systematic effects on time scales smaller than about 20 min. Weights are calculated as explained in Sect. 9.2 of [Planck Collaboration II \(2013\)](#).

In Fig. 12 we show the half-ring difference maps for the three LFI frequencies. Visual inspection of these maps shows no apparent correlated structures. A quantitative test was performed by dividing them pixel-by-pixel by the square root of the

white noise covariance maps ([Planck Collaboration ES 2013](#)) and checking the standard deviation of the resulting maps. We found this r.m.s. value to be very close to unity: 1.0211, 1.0089, and 1.0007 for 30, 44, and 70 GHz, respectively. The deviation from unity is consistent with the different level of  $1/f$  noise in the three frequency channels (see Tables 1 and 10 of [Planck Collaboration II 2013](#)).

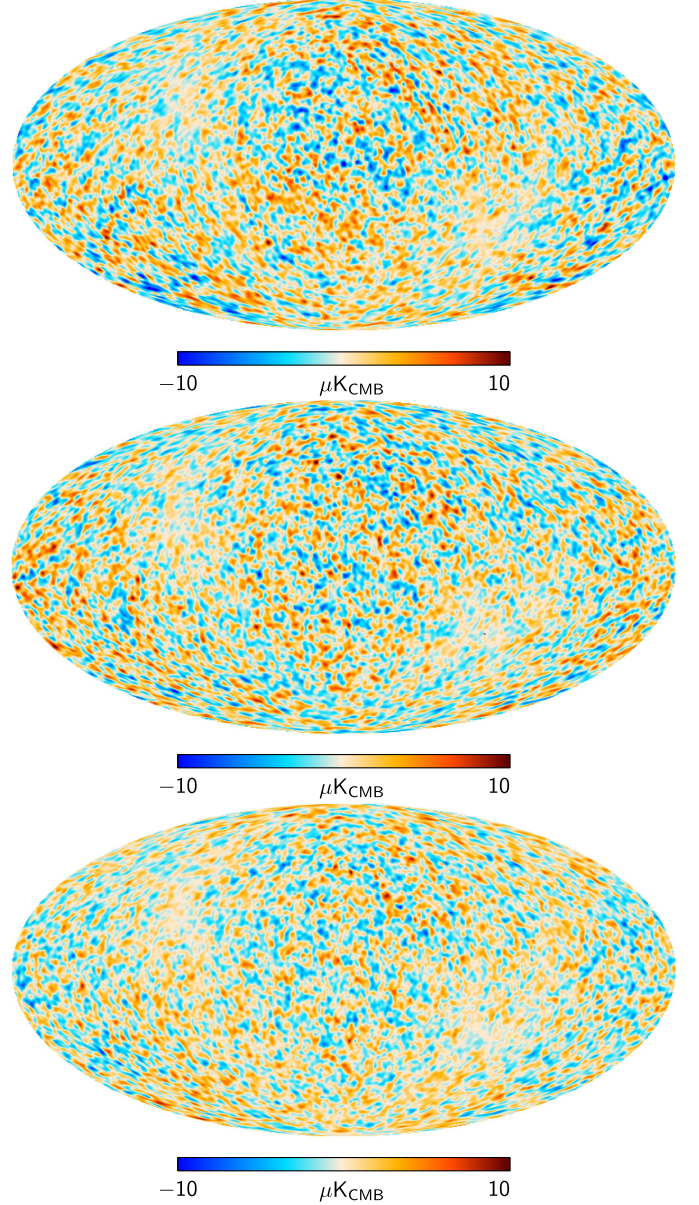


**Fig. 12.** Half-ring difference maps: 30 GHz (top), 44 GHz (middle), and 70 GHz (bottom).

##### 4.1.2. Survey difference null tests

Differences between single survey maps are useful to check for residual systematic effects at large angular scales.

Odd minus even surveys difference maps highlight effects arising from beam ellipticity and far sidelobes, as discussed in Sect. 3.2.1. In Fig. 13 we show the survey 1 minus survey 2 difference maps for the three LFI frequencies. The cosmic and orbital dipole signals are removed during calibration (as discussed



in Planck Collaboration V 2013), so the difference in orbital dipole signal between survey 1 and survey 2 is not visible. Far sidelobe pickup of the galactic plane in survey 2 is visible as a large blue ring which matches the simulation results shown in Figs. 24 through 26.

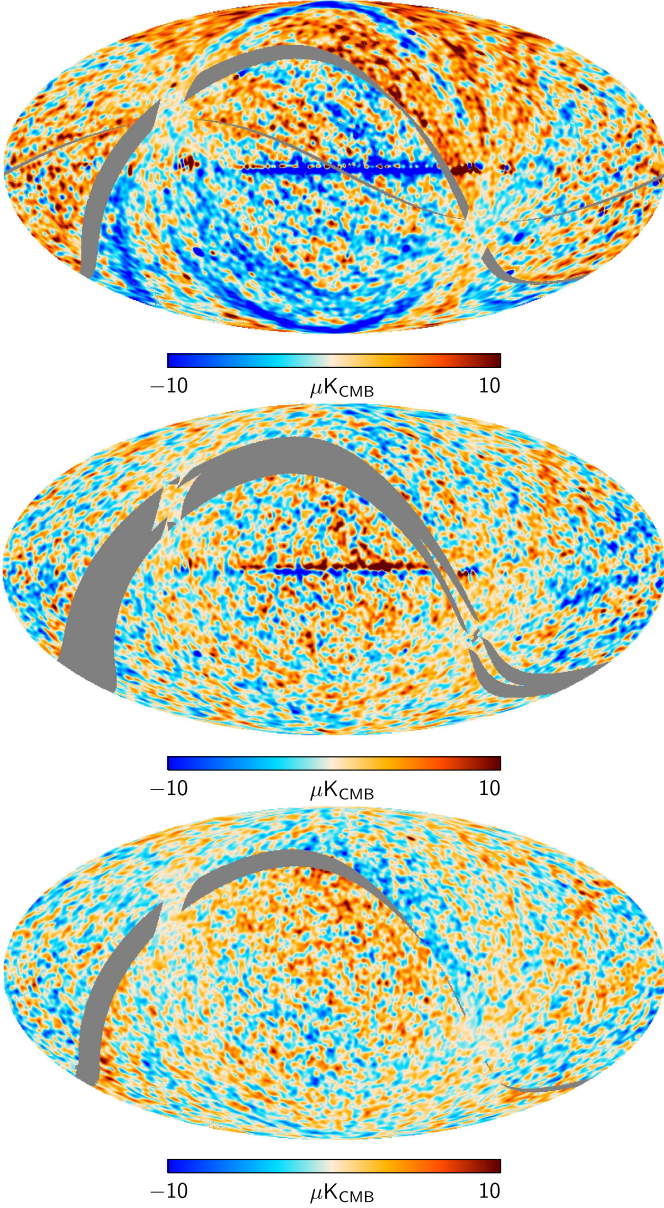


**Fig. 13.** Survey 1 minus survey 2 difference maps: 30 GHz (top), 44 GHz (middle), and 70 GHz (bottom). Such odd-even differences highlight beam ellipticity and sidelobe pickup effects.

Figure 14 shows the result of a test performed on the 30 GHz survey 1 minus survey 2 null test (first map of Fig. 13). The test consisted in removing from this map a difference map between survey 1 and survey 2 simulated sidelobes (see Fig. 24 in Sect. 4.3.1). The result (reported also in Planck Collaboration IV 2013) showed that the blue ring structure disappears, which confirms both the nature of this spurious feature in the map and that our sidelobe model is correct with a good approximation.

From the survey difference maps at the three LFI frequency bands we have estimated the r.m.s. uncertainty per pixel due to

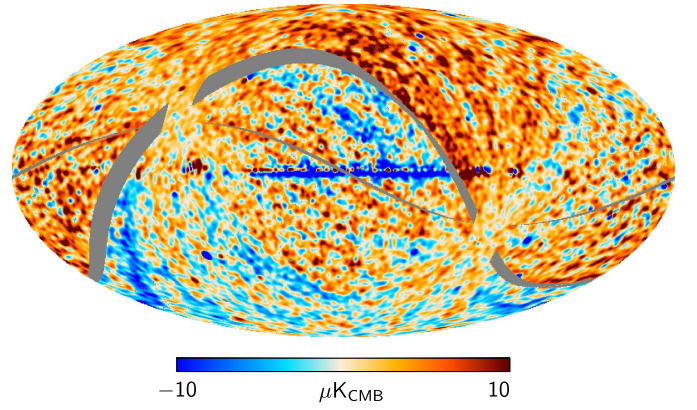


**Fig. 14.** Survey 1 – 2 difference map at 30 GHz minus the survey 1 – 2 difference map obtained from 30 GHz simulated sidelobes (Fig. 24). The blue ring disappears.

known and unknown systematic effects after correcting for the white noise contribution  $\sigma_{\text{noise}}$ . The latter has been estimated using the high- $\ell$  tail of the survey half-difference power spectra, by means of the following formula:

$$\sigma_{\text{noise}} = \sqrt{\frac{N_{\text{pix}} \langle C_\ell \rangle}{4\pi}}, \quad (2)$$

where  $N_{\text{pix}}$  is the number of pixels in the map and  $\langle C_\ell \rangle$  is the average level of the power spectrum in the white-noise dominated range  $2000 < \ell < 3000$ . This value of  $\sigma_{\text{noise}}$  quantifies the r.m.s. due to statistical noise in the survey difference maps, and it is equal to<sup>3</sup> 14.0, 16.2, and 28.1  $\mu\text{K}/\text{pixel}$  at the frequencies of 30, 44, and 70 GHz, respectively. We then use the following formula to estimate the r.m.s. due to systematic effects only (Table 2),

$$\sigma_{\text{syst}} \approx \sqrt{\sigma_{\text{sdiff}}^2 - \sigma_{\text{noise}}^2}, \quad (3)$$

where  $\sigma_{\text{sdiff}}$  is the r.m.s. of the survey difference maps. The equation holds exactly only if all the signals are gaussian, but numerical simulations have shown that Eq. (3) is true within 10-15 % for the kind of effects considered in this work.

In Fig. 15 we show survey 1 minus survey 3 null test maps. Survey 1 and survey 3 cover the sky in nearly identical orientations, and would be consistent with noise if calibration and other systematics were perfectly controlled. The visible large scale features appear to be due to the relatively poor thermal stability of the instrument for the first portion of survey 3.

We can also use angular power spectra to estimate the impact of residuals seen in our difference maps. The spectrum of the half-ring difference maps provide an accurate estimate of the noise contribution. A range of systematic effects we might be concerned about, such as imperfectly tracked gain changes, systematic thermal variations and others, might be expected to change significantly over the course of 1 year of operations. These spectra show that, to very good approximation, the signal in the survey difference maps (basically data taken six months apart) is fully explained by the instrumental noise. The fact that the half-ring difference spectra and survey difference spectra are nearly identical gives us confidence that neither the systematic effects we know about, or others we may not have anticipated, are contaminating the data in any significant way.

<sup>3</sup> The values reported here use  $N_{\text{pix}} = 12 N_{\text{side}}^2$ , with  $N_{\text{side}}$  equal to 128 (30, 44 GHz) or 256 (70 GHz).



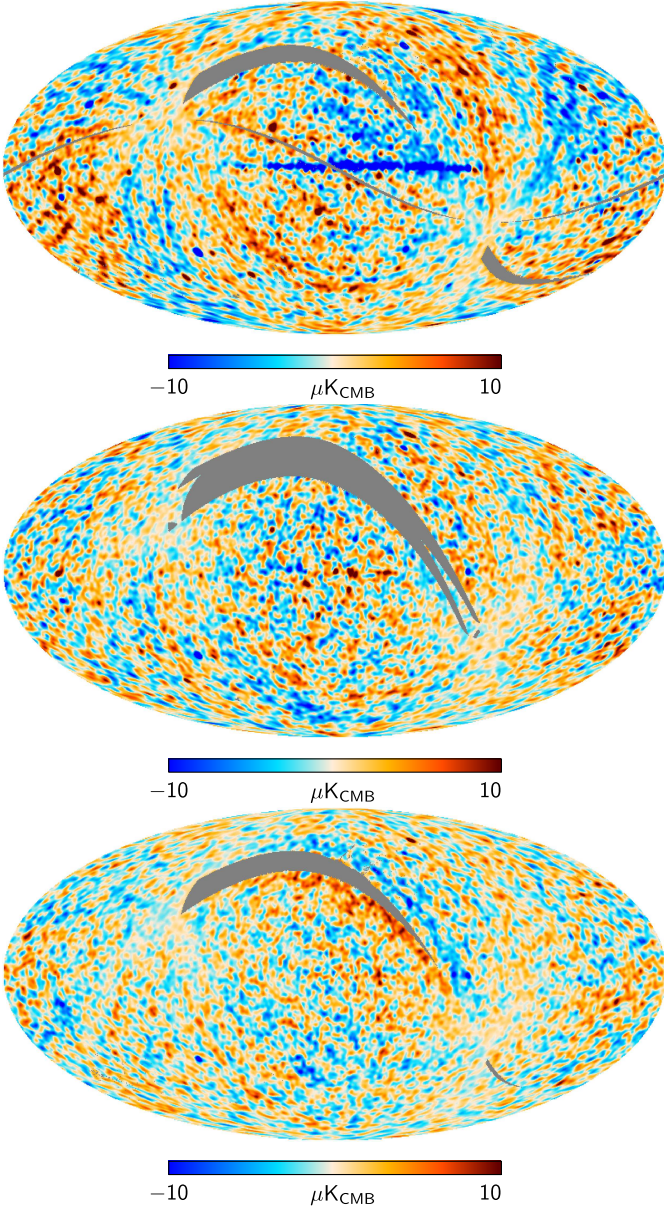


**Fig. 15.** Survey 1 minus survey 3 difference maps: 30 GHz (top), 44 GHz (middle), and 70 GHz (bottom).

## 4.2. Assessment of timeline-additive systematic effects

### 4.2.1. Thermal effects

**Method.** Thermal systematic effect maps have been generated using a simulation strategy that combines in-flight temperature sensor measurements (Mennella et al. 2010), thermal modelling of the propagation of temperature fluctuations (Tomasi et al. 2010) and radiometric transfer functions measured during ground tests (Terenzi et al. 2009). Here we sketch the procedure used to combine these data into systematic effect maps.

For each temperature effect and for each receiver detector diode we have chosen the most representative sensor, generally the closest to the receiver. Housekeeping data have been low-pass filtered to remove high frequency sensor noise, Fourier-filtered to obtain the estimated temperature fluctuation at the receiver location, and then multiplied by the radiometric transfer

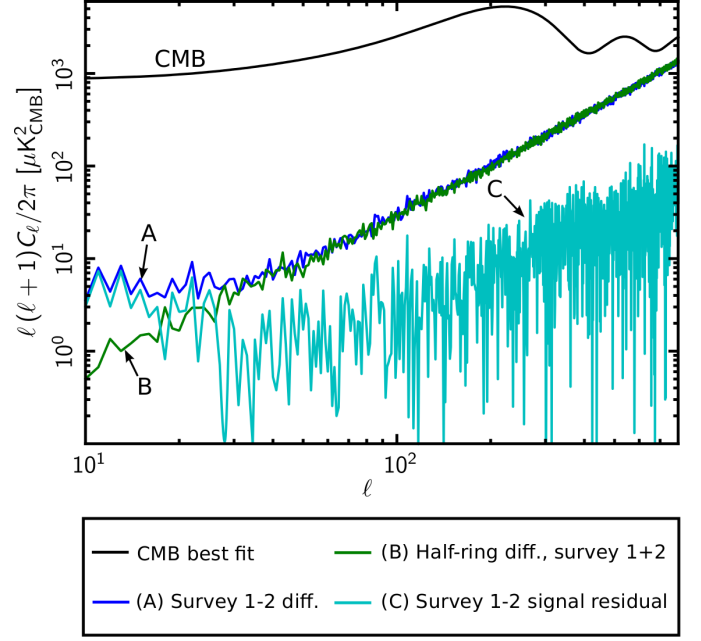


**Fig. 16.** Angular power spectra for 30 GHz null tests. Pseudo-spectra are calculated on 80% of the sky, with the Galaxy and point sources masked. All spectra are corrected for sky fraction but not for beam smearing effects. A best fit cosmological model spectrum is displayed for scale. For  $\ell > 30$  the spectrum of the survey 1 minus survey 2 map difference lies directly on top of the half-ring difference spectrum calculated for the same time period, the (absolute value) difference of these spectra is also shown. For this 30 GHz spectrum, the lower  $\ell$ s are contaminated by the sidelobe leakage at the  $20 \mu\text{K}^2$  level.

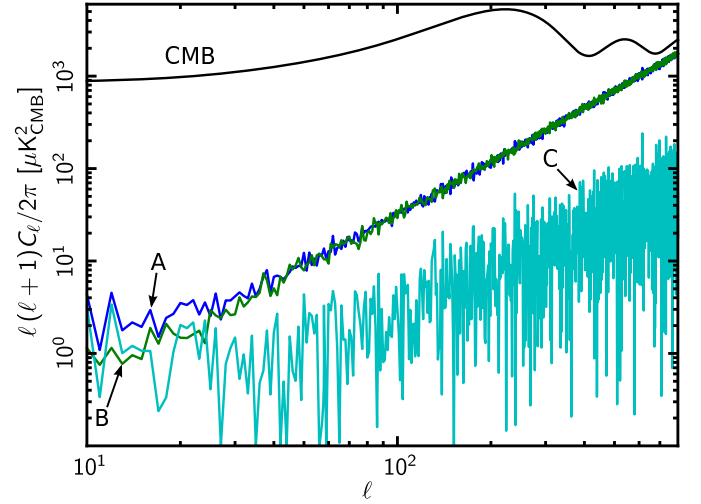


**Fig. 17.** Angular power spectra for 44 GHz null tests. For this frequency, the low  $\ell$  spectrum of the survey 1 minus survey 2 map difference is closer to that of the half-ring difference spectrum. Letters in the plot follow the same convention of the legend in Fig. 16.

function to obtain the simulated antenna temperature fluctuation on the undifferenced sky and reference load channels.

For each pointing period the average measured sky and reference load voltages have been added to the two antenna temper-

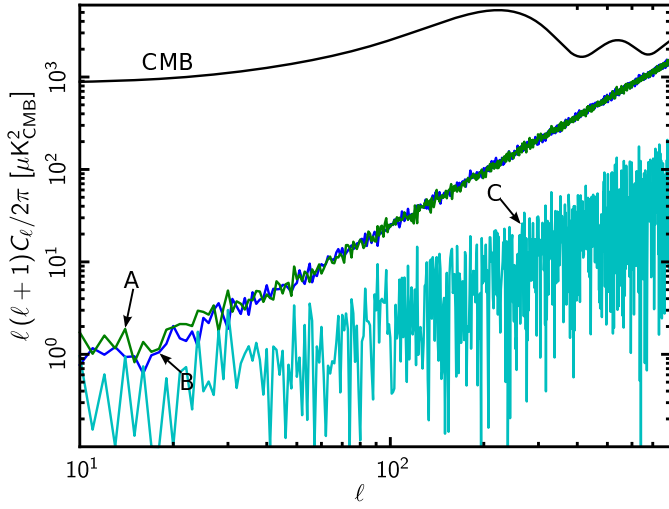


**Fig. 18.** Angular power spectra for 70 GHz null tests. At 70 GHz, the survey 1 minus survey 2 map difference and half-ring difference spectra are essentially the same everywhere. Letters in the plot follow the same convention of the legend in Fig. 16.

ature fluctuation data streams. After a weighted average of the two detector data values of each radiometer, we took the sky-load difference using the gain modulation factor,  $r$ , and multiplied the resulting stream by the photometric constant,  $G$ . The weights,  $r$ , and  $G$ , were the same as used in the nominal pipeline to produce sky maps for that radiometer.

After oversampling to the receiver sampling frequency using linear interpolation, we used these data to build maps using the in-flight pointings and the same map making procedure used to produce the final scientific products.

**Results.** In Fig. 19 we show the peak-to-peak amplitude of the various effects on final maps.

Back-end temperature fluctuations have a sub- $\mu\text{K}$  effect on maps. This low level can be understood if we consider that these fluctuations impact sky and reference load signals symmetrically and are effectively suppressed in the differential measurement. Furthermore the residual present in the data acts as a purely multiplicative effect, so that it is essentially calibrated out by applying our gain model (Planck Collaboration V 2013).

Temperature variation at the level of the 4 K reference loads couple with the radiometric output as an asymmetrical additive spurious signal. In this case the relative calibration model provides no benefit, so that at 30 and 44 GHz this effect leaves a residual of about  $1 \mu\text{K}$  peak-to-peak. The effect at 70 GHz, instead, is largely suppressed by the active thermal control system present on the HFI focal plane close to the reference loads of this frequency channel. Front-end 20 K temperature variations couple with the radiometric measurements through both gain and noise temperature fluctuations. For this reason only a part of the effect can be calibrated out. Moreover, the asymmetry of the receiver chain before the orthomode transducer is such that the effect suppression provided by the sky-load differencing is not optimal. The residual effect is similar for the three frequency channels and is of the order of  $1 \mu\text{K}$  peak-to-peak.

Maps of the combined thermal effects at the three LFI frequency channels are shown in Fig. 20.

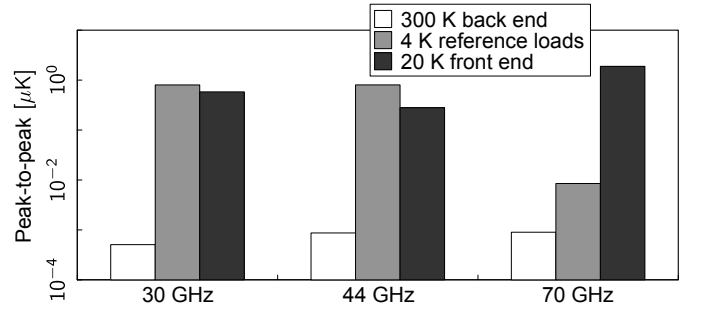


**Fig. 19.** Peak-to-peak thermal effects on maps. Notice the logarithmic scale on the ordinate axis.

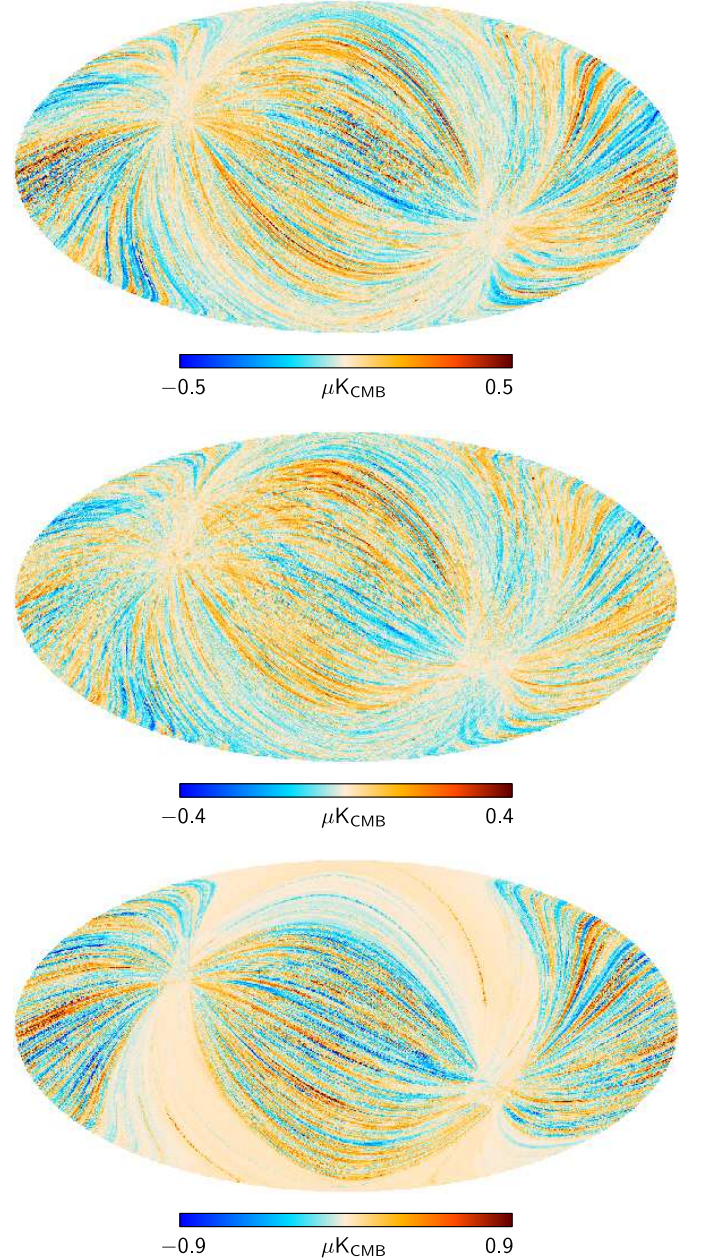


**Fig. 20.** Maps of combined thermal effects at 30 GHz (top), 44 GHz (middle), and 70 GHz (bottom).



#### 4.2.2. Bias fluctuations

**Method.** The effect of bias fluctuations in the front-end amplifiers has been computed on maps and power spectra using the measured drain currents and a linear transfer function that links the drain currents of the two amplifiers to the radiometric output in antenna temperature. Since we are interested in assessing purely electrical instabilities, we have corrected the drain current housekeeping data to remove variations induced by temperature changes in the 20 K and 300 K temperature stages, i.e.,

$$I_{\text{drain}}^{\text{corr}}(t) = I_{\text{drain}}(t) - \alpha_{20\text{K}}\delta T_{20\text{K}}(t) - \alpha_{300\text{K}}\delta T_{300\text{K}}(t), \quad (4)$$

where  $\delta T_{20\text{K}}(t)$  and  $\delta T_{300\text{K}}(t)$  are temperature variations on the 20 K and 300 K temperature units, respectively, and  $\alpha_{20\text{K}}$  and  $\alpha_{300\text{K}}$  are the corresponding drain current thermal susceptibility coefficients, which were calculated using an iterative linear fitting process. First we calculated the coefficients of the susceptibility to back-end temperature fluctuations, exploiting the temperature change induced by the change in the transponder state, which occurred at day 258 (see Fig. 7), and then we determined the coefficients of the susceptibility to front-end temperature fluctuations using data from a temperature susceptibility test run at the end of the in-flight calibration phase. The iterative process was closed by re-calculating back-end thermal coefficients after correcting drain currents for front-end temperature fluctuations.

After thermal correction we correlated drain current changes with antenna temperature variations in sky and reference load samples. We recall here that the LFI receiver architecture implies that the signal characteristics at each detector depend on both the radiometer front-end amplifiers (Bersanelli et al. 2010). So, for each detector diode we have first calculated the weight,  $w$ , providing the maximum correlation between the output voltage and the linear combination of the drain currents of the two radiometer amplifiers, then a linear fit between this combination and the voltage output provided the required transfer function. Mathematically the relationship between the corrected drain current fluctuations ( $\delta I_{\text{drain}}^{\text{corr}}$ ) and the voltage output variations ( $\delta V_{\text{sky(ref)}}$ ) reads:

$$\delta V_{\text{sky(ref)}}(t) = \alpha_{\text{sky(ref)}} \left[ w \delta I_{\text{drain},1}^{\text{corr}}(t) + (k - w) \delta I_{\text{drain},2}^{\text{corr}}(t) \right], \quad (5)$$

where  $k$  is a constant,  $w$  is the weight and  $\alpha_{\text{sky(ref)}}$  is the slope of the linear fit between the weighted combination of the two drain currents and the sky (reference load) voltage outputs. The time-ordered data obtained by Eq. (5) have then been projected onto the sky using flight pointings.

**Results.** Maps of the residual effect arising from bias fluctuations are shown in Fig. 21. This residual effect is less than  $1\text{ }\mu\text{K}$  peak-to-peak at all frequencies and presents little structure apart from a stripe in the 70 GHz map, that is caused by a jump in the bias voltage that occurred at day 258, following the change in transponder state. This jump affected more the 70 GHz radiometers so that a small signature was left in the maps.

#### 4.2.3. 1-Hz spikes

**Method.** Time ordered data containing the spike signal have been generated using templates obtained from flight radiometric data. The details of this method have been described in Sect. 7.1 of Mennella et al. (2011) and will not be repeated here.

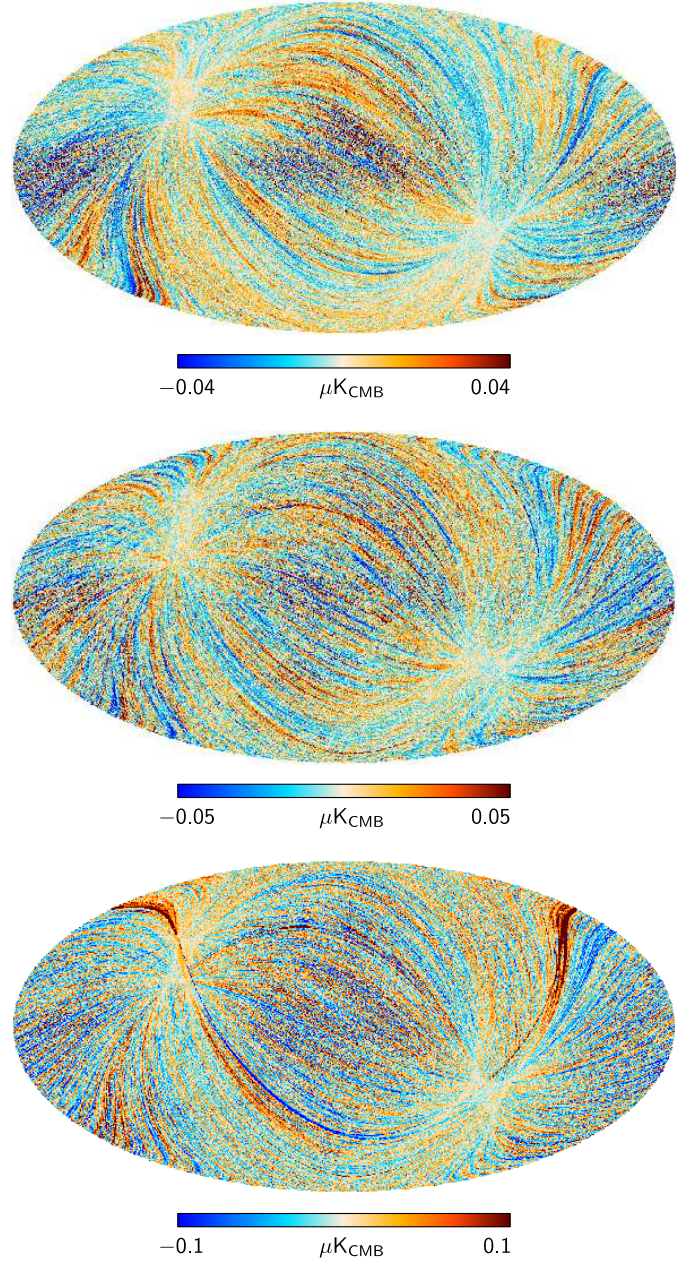


**Fig. 21.** Maps of the effect from drain current fluctuations at 30 GHz (top), 44 GHz (middle) and 70 GHz (bottom).

**Results.** In Fig. 22 we show maps of the spike systematic effect at the three LFI frequencies. Because, as described in Planck Collaboration II (2013), spikes are removed from 44 GHz but not from 30 and 70 GHz time-ordered data, the corresponding maps represent the residual effect after removal at 44 GHz and the spike effect with no removal applied at 30 and 70 GHz. In all the three channels the r.m.s. effect is at the sub- $\mu\text{K}$  level.

### 4.3. Assessment of effects dependent on the sky

#### 4.3.1. Sidelobes

**Method.** The external straylight contamination has been evaluated with simulations in which the sky model includes the diffuse Galactic emission and the dipole, which are the most important sources of external straylight contamination. At 30 GHz, the straylight contamination has been assessed including the beam



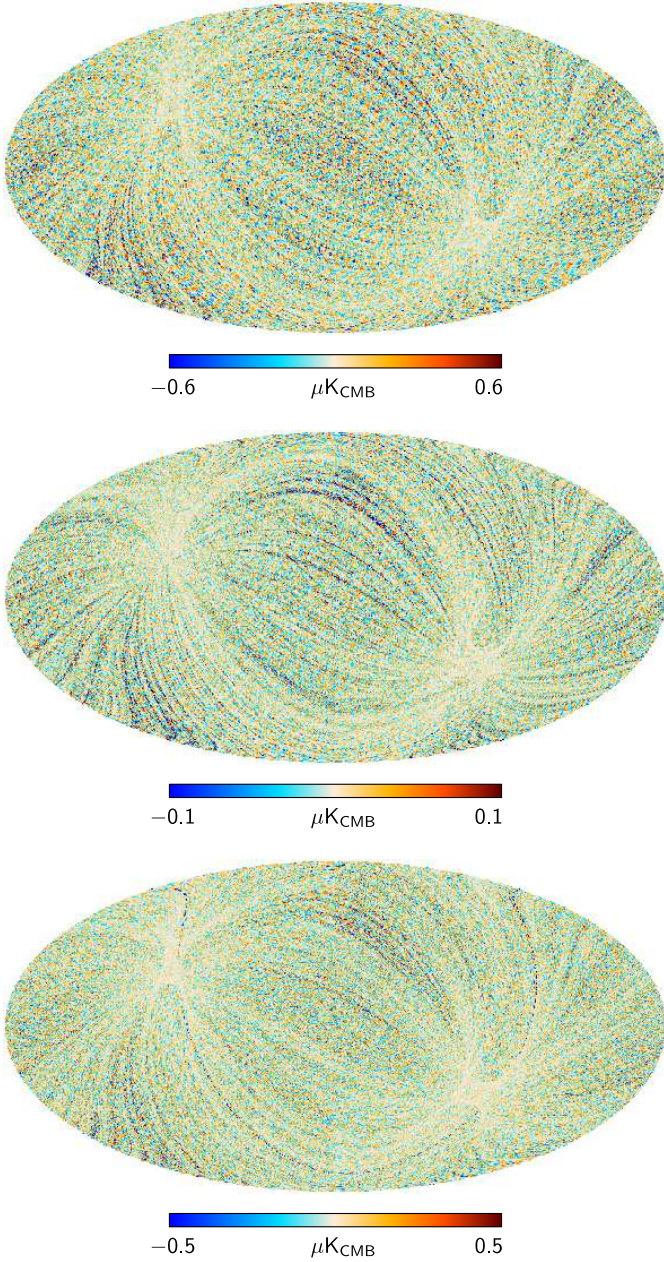


**Fig. 22.** Maps of 1 Hz spikes at 30 GHz (top), 44 GHz (middle) and 70 GHz (bottom). The map at 44 GHz represents the residual after the spike signal has been removed from the time-ordered data, while maps at 30 and 70 GHz represent the spike signal with no removal applied.

frequency dependence and the receiver in-band response. The bandpass response (Zonca et al. 2009) of the radiometers was divided into discrete frequency intervals. For each frequency interval a weight factor was calculated as the integral of the bandpass response over the interval itself. In Fig. 23 we show, as an example, the bandpass response of the LFI27 receiver (main and side arms) and the seven frequency intervals considered in the simulations. The weights correspond to the integral of the bandpass response curve over the frequency interval.

In parallel, far sidelobes were computed using the GRASP MrGTD<sup>4</sup> software ([www.ticra.com](http://www.ticra.com)) at the frequencies indicated on the top of each slice reported in Fig. 23 (27, 28, 29, 30, 31,

<sup>4</sup> Multi-reflector geometrical theory of diffraction

32, and 33 GHz). The optical model used in GRASP simulations is the “RFTM” reported in Planck Collaboration IV (2013).

For each frequency interval an observation of the sky model was simulated for all 30 GHz detectors using the beam sidelobes and the real sky pointings, neglecting beam smearing effects and weighting the data stream with the above mentioned weight factors. Finally the Madam map-making code was run to generate maps from simulated data streams.

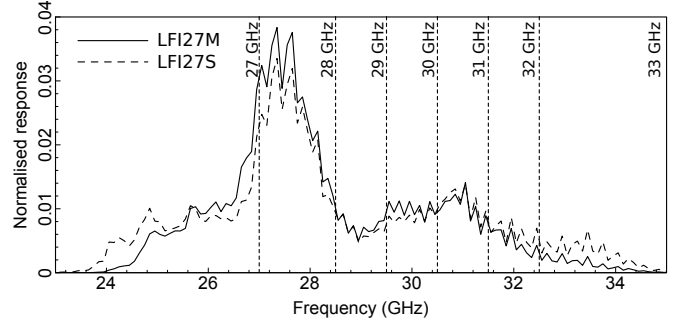


**Fig. 23.** Bandpass response of the two radiometers of the LFI27 receiver. The figure shows the seven frequency intervals and the corresponding frequencies at which sidelobes have been simulated. For each interval the weight is the integral of the bandpass response curve.

**Results.** In Fig. 24 through 26 we show the simulated sidelobe fingerprint on the sky, after the destriping process, for the odd surveys (left side) and even surveys (right side), respectively. The figures show that the straylight from the cosmological dipole is similar in the two surveys, while the Galaxy straylight is larger in the second survey, as expected. The ring-shaped fingerprint in the second survey has also been revealed at the expected level in the real data by taking the difference of even minus odd survey maps (see Figs. 13 and 14 in Sect. 4.1), thus confirming the reliability of our simulations.

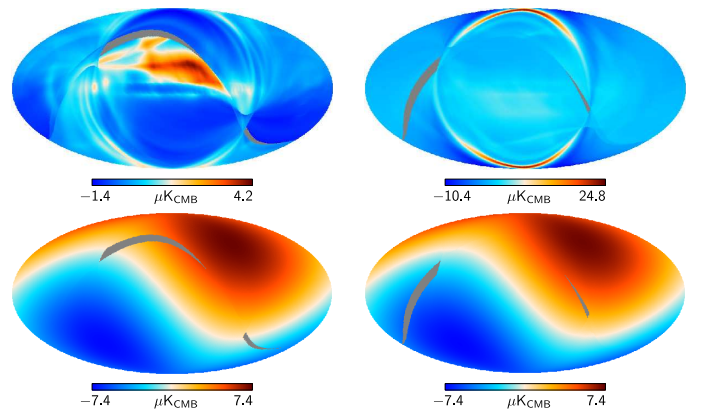


**Fig. 24.** 30 GHz channel: sidelobe fingerprint on the sky due to Galactic foregrounds (top row) and cosmological dipole (bottom row). Survey 1 (left side) and survey 2 (right side).

Results show that the most sensitive channel to straylight is 30 GHz, followed by 70 GHz and 44 GHz, which is the most insensitive channel to straylight effects. This is consistent with the

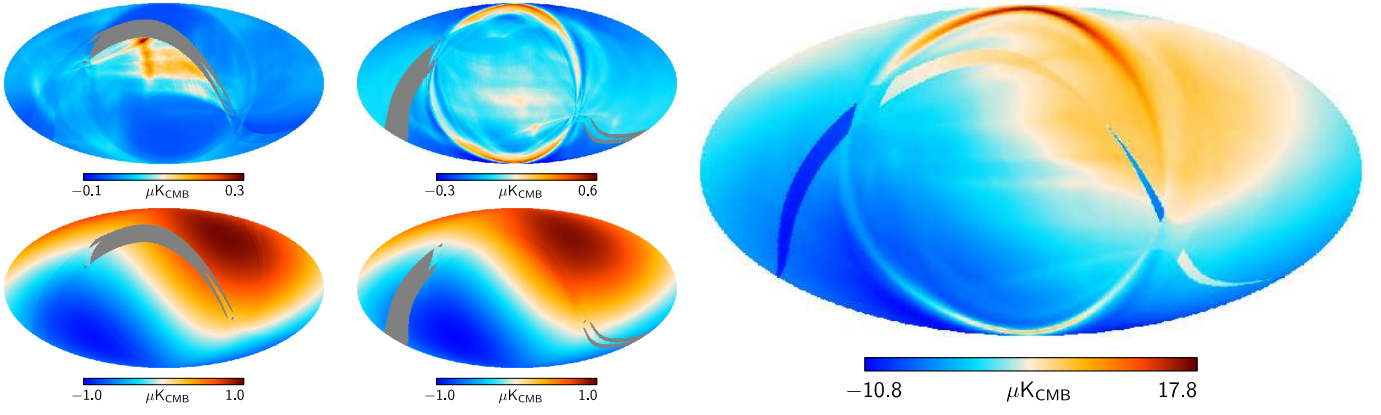


**Fig. 25.** 44 GHz channel: sidelobes fingerprint on the sky due to Galactic foregrounds (top row) and cosmological dipole (bottom row). Survey 1 (left side) and survey 2 (right side).

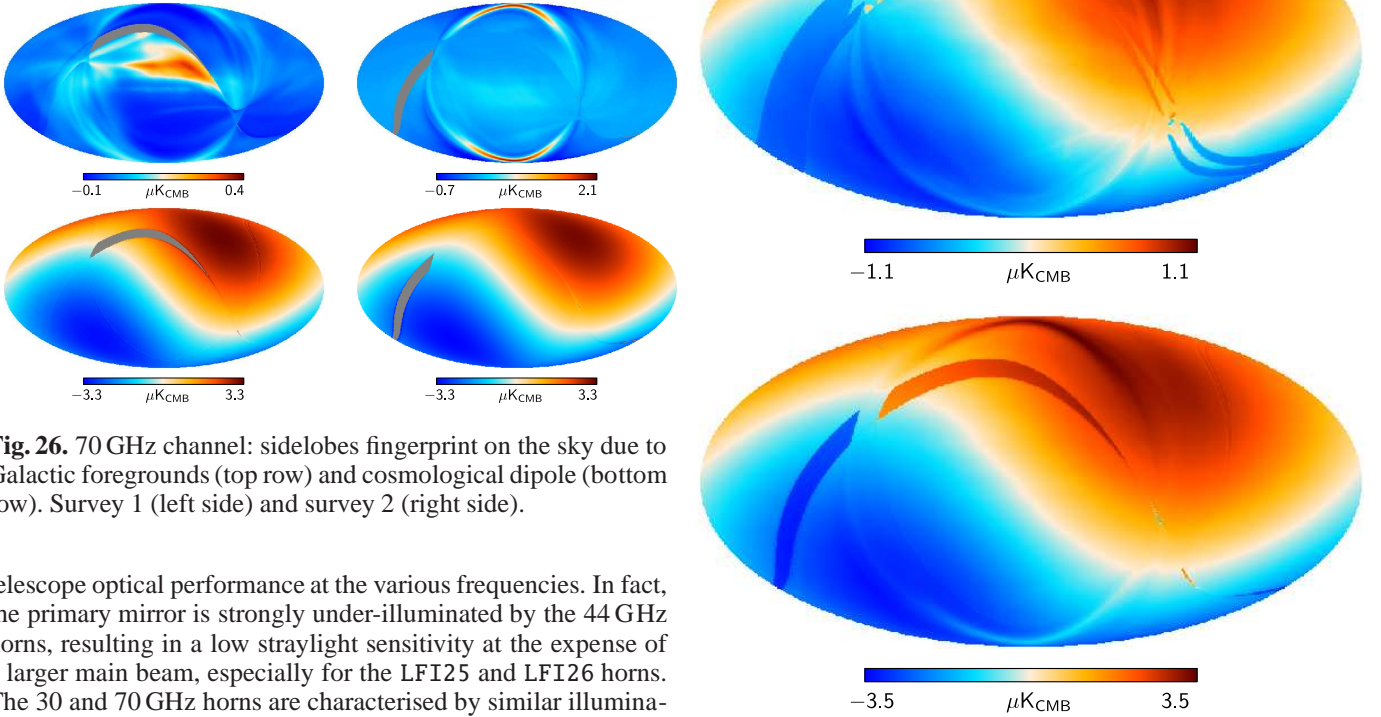


**Fig. 26.** 70 GHz channel: sidelobes fingerprint on the sky due to Galactic foregrounds (top row) and cosmological dipole (bottom row). Survey 1 (left side) and survey 2 (right side).

telescope optical performance at the various frequencies. In fact, the primary mirror is strongly under-illuminated by the 44 GHz horns, resulting in a low straylight sensitivity at the expense of a larger main beam, especially for the LFI25 and LFI26 horns. The 30 and 70 GHz horns are characterised by similar illumination properties, so that their straylight susceptibilities are comparable, with a slightly better performance of the 70 GHz horns with respect to the 30 GHz ones. If we also take into account the larger sensitivity of the 30 GHz channel to the Galactic signal it is apparent that this channel is, overall, the most susceptible to straylight contamination.

Finally, to quantify the straylight effect on maps and power spectra, we have generated a global map per frequency, including the dipole and Galactic straylight signals for both surveys (see Fig. 27).

#### 4.3.2. ADC non-linearity

**Method.** The levels of the residuals due to ADC correction process were estimated by applying the correction algorithm to simulated data containing a known ADC effect and making difference maps with those produced from data with no ADC effect. Ring-based sky and reference load time-ordered data for all individual detectors were constructed. The noise component was estimated using average  $1/f$  noise parameters over the nominal mission for each detector. Galactic and CMB signals were represented by using the observed maps, which were rolled out in the time-ordered data using real pointings and successively uncalibrated using the inverse of the appropriate gain table. The same was done with a map of the *WMAP* dipole, while the orbital dipole was calculated from the pointing information and JPL ephemeris for the satellite velocity. Finally spline fits to the observed sky and reference voltage levels per pointing period were used together with estimated receiver temperatures,  $T_{\text{CMB}} = 2.725$  K and  $T_{\text{ref}} = 4.5$  K, as a model for the gain evolution.

**Fig. 27.** Straylight contamination maps at 30 GHz (top), 44 GHz (middle) and 70 GHz (bottom).

resented by using the observed maps, which were rolled out in the time-ordered data using real pointings and successively uncalibrated using the inverse of the appropriate gain table. The same was done with a map of the *WMAP* dipole, while the orbital dipole was calculated from the pointing information and JPL ephemeris for the satellite velocity. Finally spline fits to the observed sky and reference voltage levels per pointing period were used together with estimated receiver temperatures,  $T_{\text{CMB}} = 2.725$  K and  $T_{\text{ref}} = 4.5$  K, as a model for the gain evolution.

An ADC effect was induced by applying the inverse of the spline correction used in the real data. The same algorithm as used with the real data was applied to the simulated data iteratively five times to ensure convergence. Intensity maps were constructed just using a simple binning of the data into an  $N_{\text{side}} = 1024$  map at each iteration and also to data with no



ADC effect added. Some of these maps showed a residual dipole caused by small changes in the overall slope of the temperature-voltage response curve due ADC correction. Since the calibration pipeline will determine this response and not give rise to a residual dipole, we also remove it here via a correlation fit with the input dipole map. The ADC effect maps are then the difference between the fifth iteration map and the no-ADC map. Maps for each frequency band are then produced by averaging all maps for that frequency, taking into account the detector weighting.

Since not all the 70 GHz channels could be corrected due to some channels having “popcorn” noise, another method was used to estimate the likely level of ADC error, using the white noise level on the difference data. This is immune to the “popcorn” noise, but cannot be used to correct the ADC effect, since it is not known whether the effect is on the sky or reference voltages. In this case we only estimate the ADC effect and do not apply any correction.

**Results.** Maps of the ADC effect at the three LFI frequency channels are shown in Fig. 28. The main effect of the ADC residuals is a small ( $< 0.1\%$  of the dipole signal) ring-based gain error which appears in the maps as stripes in the scan direction. The residuals are generally larger where the strongest signals are: the dipole and Galactic plane. The contribution from the Galactic plane becomes weaker at higher frequencies as expected. Broad stripes seen in the 30 GHz map are due to residual deviations from linearity on voltages ranges larger than the ADC peaks. These also occur at the other frequencies, but as the number of channels increases this effect averages out, leaving more uniform noise-limited, low-level residuals at 70 GHz. While the 44 GHz channels have the strongest ADC effect due to lower detector voltages, they are also the best characterized, leading to a well-determined correction placing it between 30 and 70 GHz in terms of the amplitude of residuals.

#### 4.3.3. Imperfect photometric calibration

**Method.** We have developed an analytical model of the impact of the uncertainty in the dipole calibration algorithm due to the radiometer white noise and the loss of integration time due to Galactic masking. We have run this model to estimate how this effect propagates through the calibration and mapmaking pipeline. Such simulations scan a sky map (the *input map*) of pure astrophysical signal (without dipole) to produce a time-ordered data stream, which is then uncalibrated using gains inferred from the total-power output of the radiometers. These time-ordered data are then used as input in a simplified version of the LFI pipeline to produce a new calibrated map (the *output map*). The difference between the input and output maps should be mainly due to dipole leakage, since the gains used in the de-calibration phase differ from those calculated by the pipeline. Refer to Sect. 5 in (Planck Collaboration V 2013) for more information.

**Results.** Fig. 29 shows the difference between the input and output maps. The shape of the features in these maps closely follows the scanning circles drawn by the pointing direction of the telescope towards the sky. (This is expected, since the calibration is performed on the time-ordered data.) The estimated impact of such systematic effects on the *Planck*-LFI maps is of the order of a few  $\mu\text{K}$  per pixel.

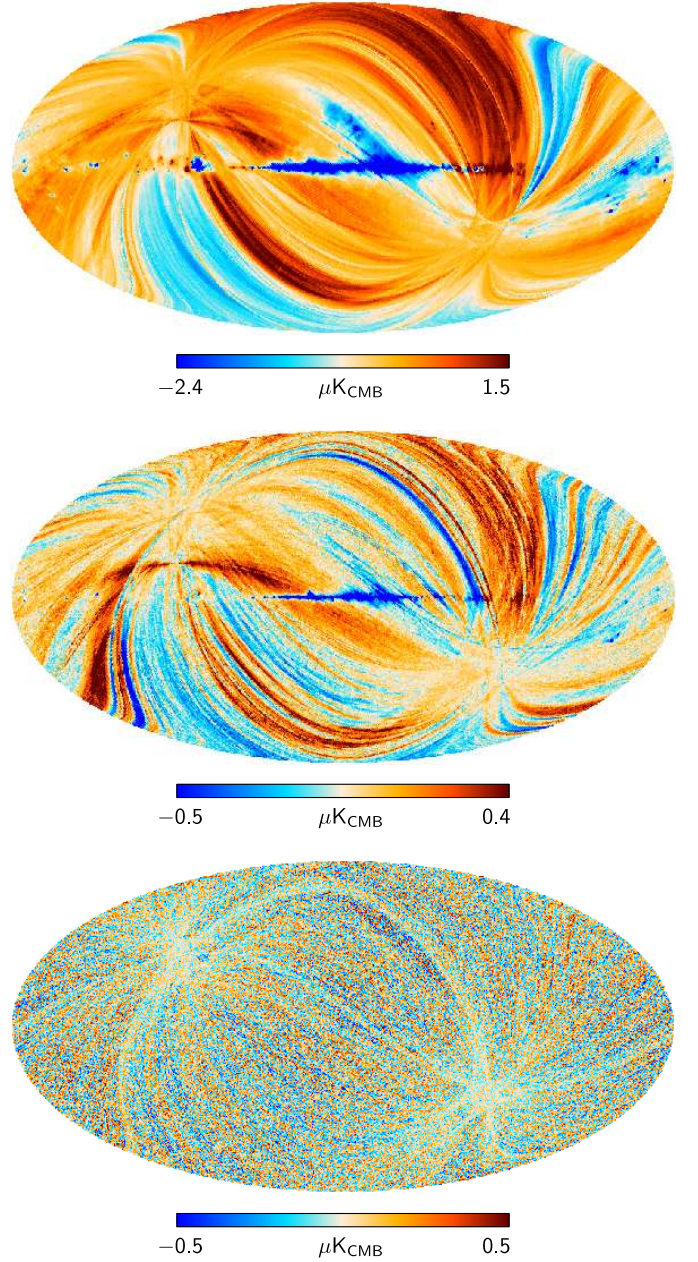


**Fig. 28.** Maps of the ADC non-linearity effect at 30 GHz (top), 44 GHz (middle), and 70 GHz (bottom).

#### 4.4. Pointing uncertainties

**Method.** To estimate the uncertainty introduced by the Gaussian fit in main beam measurements we performed tests using the radio-frequency model of the flight telescope (Planck Collaboration IV 2013) and we compared the centre calculated by the fit with the beam maximum, which is uniquely determined in optical simulations. Typical differences between the centres are  $1''$  for all the 70 GHz beams,  $4''$  for LFI24,  $18''$  for LFI25 and LFI26 (44 GHz horns), and  $6''$  for the beams at 30 GHz. All these estimates are less than the statistical uncertainty in the determination of the beam centre, which ranges from  $4''$  at 70 GHz to  $10''$  at 30 GHz.

The focal plane geometry was reconstructed using four Jupiter transits labelled as J1, J2, J3 and J4 (Planck Collaboration II 2013; Planck Collaboration IV 2013). When we compared the focal plane geometry obtained from the combination of J1 and



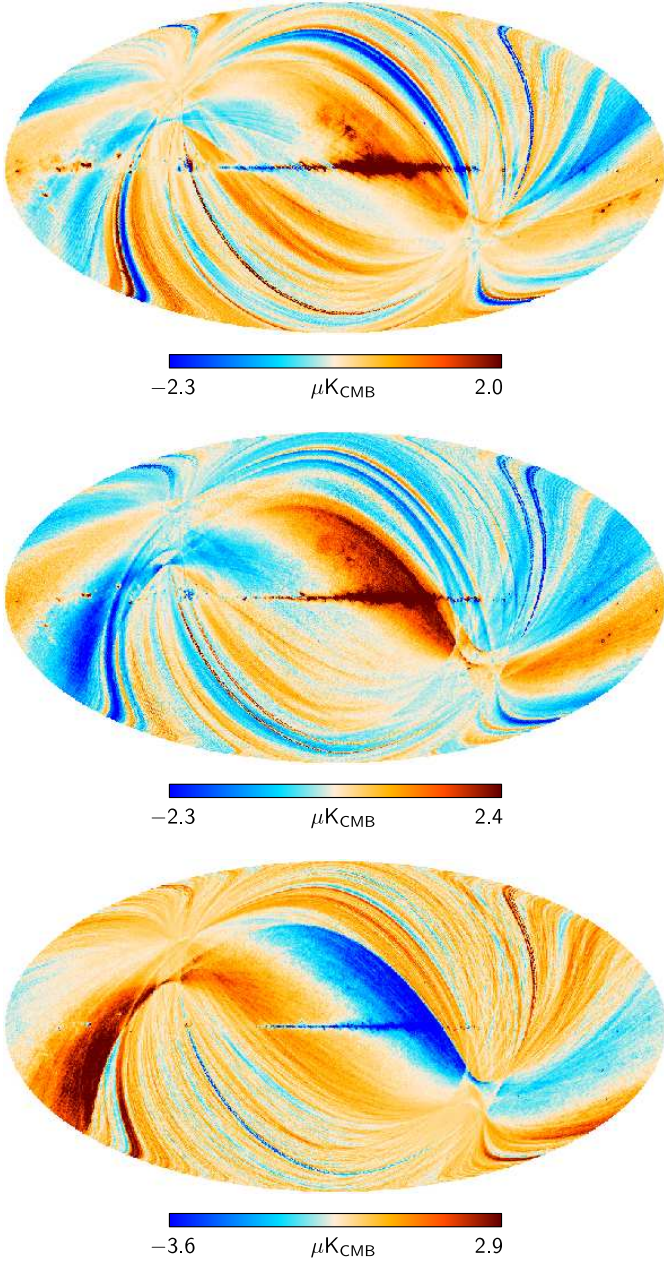


**Fig. 29.** Maps of the effect of calibration uncertainties at 30 GHz (top), 44 GHz (middle), and 70 GHz (bottom).

J2 with the one obtained from the combination of J3 and J4 we found a difference of about  $15''$  in pointing, mainly along the in-scan direction. On the other hand, the comparison of the focal plane geometries determined from single Jupiter transits (J1 against J2 and J3 against J4) showed differences within the expected uncertainty. The  $15''$  discrepancy, likely to be correlated with changes in the thermal control set-point of the data processing unit in the instrument digital electronics, was compensated using two different instrument databases in the data analysis pipeline, one for the period ranging from day 91 to day 539 after launch, and the other for the period between day 540 and day 563. Details of the focal plane reconstruction and related uncertainties can be found in [Planck Collaboration II \(2013\)](#).

We checked the impact of this effect using dedicated simulations according to the following procedure:

1. generate time ordered data by observing a CMB-only sky with flight detector pointing derived by applying the two focal plane database solution;
2. reconstruct the CMB map from the time-ordered data generated in step 1 applying the two focal plane database solution in map reconstruction;
3. repeat step 2 using the single focal plane database solution;
4. take the difference of the power spectra obtained from the two generated maps.

**Results.** Figure 30 shows that the relative difference of power spectra obtained from the two maps generated according the above procedure is of the order of  $10^{-4}$ , which is negligible.

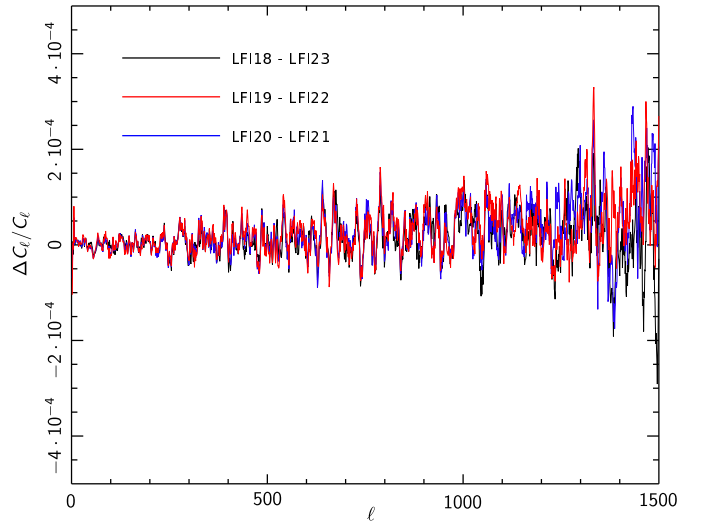


**Fig. 30.** Relative difference between the spectra of the maps simulated with one and two instrument databases. The three curves represent power spectra relative to three different feed horn pairs in the 70 GHz frequency channel. A running average smoothing has been applied to reduce the scatter and enhance any larger-scale trends. The order of magnitude of relative uncertainties is  $\Delta C_\ell/C_\ell < 10^{-4}$ .

#### 4.5. Propagation of systematic uncertainties in component separation

A further step in our assessment has been to evaluate the impact of the various systematic effects on the CMB map independently from the frequency. In order to do this we have weight-summed the three maps for each effect using weights obtained using a pixel-based ILC (internal linear combination) component separation ([Leach et al. 2008](#); [Planck Collaboration XII 2013](#)). ILC relies on variance minimisation exploiting a multi-frequency dataset including a flat spectrum CMB component in thermodynamic temperature plus foregrounds characterized by a non-thermal spectrum. With this approach the CMB temperature can be determined at each pixel,  $p$ , by a simple weighted sum of the frequency maps once the correct weights are found:

$$T_{\text{CMB}}(p) = \sum_{i=1}^N w_i T_{\nu_i}(p),$$

$$\sum_{i=1}^N w_i = 1. \quad (6)$$

The propagation of systematic effects in component separation can be assessed using Eq. (6), in which we use the systematic effect maps at the various frequencies instead of the measured frequency maps. Therefore, for each pixel, we have that the residual systematic effect after component separation will be given by

$$T_{\text{syst}}(p) = \sum_{i=1}^N w_i T_{\text{syst}, \nu_i}(p), \quad (7)$$

where the set of weights  $w_i$  is the same as used for retrieving the CMB map. In our assessment we have considered only LFI systematic effects and so we assumed, in Eq. (7),  $T_{\text{syst}, \nu_i} = 0$  for  $\nu_i > 70$  GHz. For the simplicity of this estimation, the weights are uniformly distributed in pixel and harmonic domains. In the *Planck* component separation pipeline, the variance minimisation is conducted in the needlet space, i.e., on sub-sets of the harmonic and pixel domains where foregrounds are relevant at various levels, resulting in a set of coefficients for each needlet domain (Planck Collaboration XII 2013).

#### 4.6. Gaussianity statistical tests

We now assess non-Gaussianity induced by the systematic effects on the LFI data maps. We present results on different non-Gaussianity tests carried out on maps containing the various systematic effects considered through the paper. In particular, we studied the map obtained by summing all the systematic effect maps.

For detailed information on the non-directional or targeted non-Gaussianity tests on the Planck data see, for example, Planck Collaboration XXIII (2013), Planck Collaboration XXIV (2013), and Planck Collaboration XIX (2013). The list of estimators for the non-Gaussianity tests is based on a selection of well-known statistics that are able to detect non-Gaussian signals with a wide range of amplitude and morphological properties. In particular we consider the Minkowski functionals (Schmalzing & Gorski 1998), statistical quantities derived from the 1-point PDF (variance, skewness, kurtosis and the Kolmogorov-Smirnov or KS distance) and the skewness and kurtosis of the spherical Mexican hat wavelet (SMHW, Martínez-González et al. 2002). The properties of these estimators are described in Planck Collaboration XXIII (2013) and references therein.

We have compared values of our estimators applied to a set of realistic Gaussian CMB and noise realizations and another set based on the same CMB and noise simulations summed with the systematic effect maps. The CMB and noise maps were simulated following the *Planck*-LFI data processing pipeline (Planck Collaboration II 2013). Where the three estimators did not provide significant deviations between the maps with and without the systematic effects, we have carried out an additional test by rescaling the systematic effect maps with a constant factor in order to provide an estimate of the needed amplitude to detect significant deviations with respect to the CMB signal (larger than  $3\sigma$  or 99% confidence level).

**Table 3.** Impact of systematic effects on mean 1-point PDF estimators

Frequency [GHz]	30	44	70
Standard deviation	-0.07	-0.01	-0.01
Skewness . . . . .	-0.02	-0.01	-0.01
Kurtosis . . . . .	-0.02	0.00	-0.01

Figure 31 shows the three Minkowski functionals for the three LFI frequency bands. In each panel we compare the  $\pm 1\sigma$  (68%) confidence band centred on the mean corresponding to the Gaussian CMB plus noise simulations, with the same simulations with systematic effects added for HEALPix resolutions  $N_{\text{side}} = 512, 256$ , and 128. Our analysis shows that the estimators based on the Minkowski functionals are not affected by the presence of systematic effects in the maps.

Table 3 contains the difference of the mean of the two distributions (maps with and without systematic effects) normalized by its dispersion corresponding to the four statistics based on the 1-point PDF, namely standard deviation, skewness, kurtosis and KS distance for the three LFI frequency bands. The maps are at HEALPix resolution of  $N_{\text{side}} = 1024$ . There are no significant deviations, the distributions corresponding to the two types of map are almost superimposed and therefore the estimators based on the 1-point PDF are not affected by systematic effects.

Table 4 contains the difference of the mean of the two distributions (maps with and without systematic effects) normalized by its dispersion and corresponding to the skewness and the kurtosis of the SMHW for the LFI frequency bands. The maps have a HEALPix resolution of  $N_{\text{side}} = 1024$ . The list of angular scales selected for this analysis is the one used in Planck Collaboration XXIV (2013) for the  $f_{\text{nl}}$  estimation, and it is based on a set of 16 angular scales between  $1.3'$  and  $956.3'$  logarithmically spaced. There are no significant deviations and therefore also the estimators based on the SMHW are not affected by systematic effects.

Finally we have characterized the levels of detectability of the non-Gaussian contamination of these systematic effect maps. Using the statistics based on the 1-point PDF and the Minkowski functionals, we have analysed simulations with different levels of systematic effects:

$$\Delta T(\mathbf{n}) = \Delta T_{\text{CMB}}(\mathbf{n}) + \Delta T_{\text{noise}}(\mathbf{n}) + f \Delta T_{\text{syst}}(\mathbf{n}), \quad (8)$$

where  $f$  is a factor that measures the level of detectability. We consider that the non-Gaussian signal is detected for the value of  $f$  for which any of the estimators is outside the  $3\sigma$  confidence level of the values corresponding to maps without systematic effects. The results indicate that the minimum value of the factor  $f$  beyond which we detect non-Gaussianity is:  $f \sim 8$  at 30 GHz,  $f \sim 12$  at 44 GHz, and  $f \sim 7$  at 70 GHz. In summary, systematic effects do not generate significant levels of non-gaussianity for the temperature maps at the three LFI frequencies.

## 5. Conclusions

In this paper we have analysed and quantified the uncertainties on *Planck*-LFI CMB temperature anisotropy measurements arising from systematic effects. The analysis has been fulfilled using two complementary approaches.

Firstly we adopted a *top-down* approach, in which spurious excess signals were highlighted by a series of dedicated null-tests in which maps containing the same sky signal were differenced to obtain maps containing noise and systematic effect

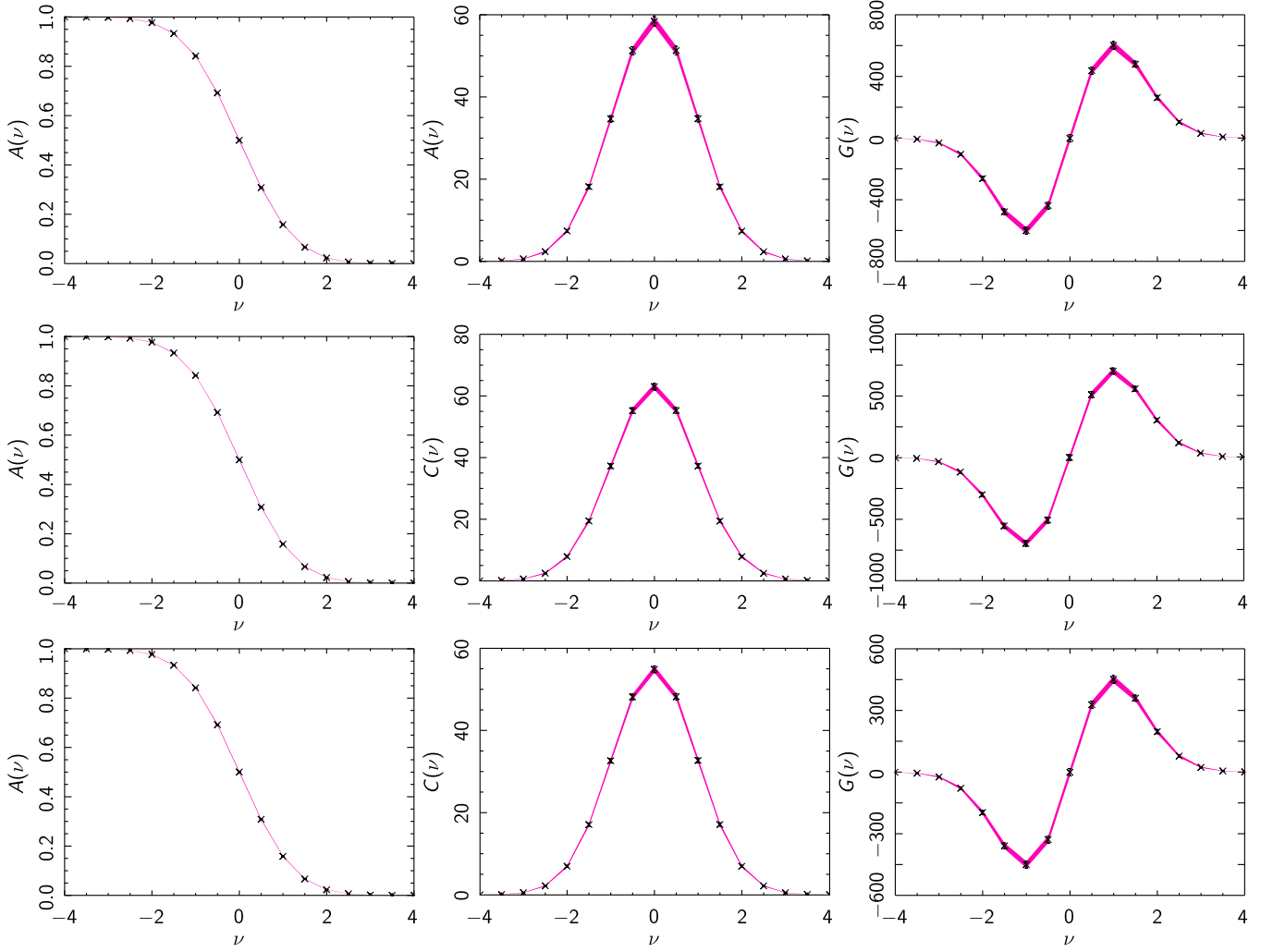


**Fig. 31.** The three Minkowski functionals computed for Gaussian CMB and noise simulations (black symbols) compared with the Minkowski functionals computed for the same simulations with systematic effects added (solid magenta line). From left to right: the area, contour length or perimeter, and the genus. From top to bottom: the three LFI frequencies, 30, 44, and 70 GHz. These are explicitly for:  $N_{\text{side}} = 512$ .

residuals. Secondly we followed a *bottom-up* approach in which each effect has been simulated to produce timelines and maps which have been further propagated through ILC component separation to a frequency-independent map.

Our analysis has shown that systematic effect uncertainties are two orders of magnitudes or less below the CMB temperature anisotropy power spectrum, and are dominated by straylight pick-up from far sidelobes and imperfect photometric calibration. In this current data release the sidelobe signal is not removed from the data, but the CMB dipole pickup by far sidelobes is accounted for during the calibration process using a monochromatic model.

Statistical analyses performed on maps containing the sum of all the simulated systematic effects added to a simulated CMB map showed no detectable non Gaussianity levels unless their level was artificially increased by a factor ranging from 7 to 12, which confirms that instrumental effects do not significantly impact Gaussianity studies.

Comparison of power spectra obtained via the *top-down* and *bottom-up* approaches show a signal excess in the survey difference maps at 30 GHz that is not accounted for in the simu-

lated maps, in the multipole range  $\ell < 20$ . This excess could be caused by yet un-modelled straylight pick-up affecting the measurements both directly and in the photometric calibration process.

Currently, analysis focusses on understanding and further reducing the level of systematic uncertainties in view of the 2014 data release which will include polarization data and results. Areas of activity include a more thorough in-band modelling of the sidelobe response at all frequencies aimed at removing the spurious signal from timelines and at a better correction during the calibration step.

**Acknowledgements.** The development of Planck has been supported by: ESA; CNES and CNRS/INSU-IN2P3-INP (France); ASI, CNR, and INAF (Italy); NASA and DoE (USA); STFC and UKSA (UK); CSIC, MICINN, JA and RES (Spain); Tekes, AoF and CSC (Finland); DLR and MPG (Germany); CSA (Canada); DTU Space (Denmark); SER/SSO (Switzerland); RCN (Norway); SFI (Ireland); FCT/MCTES (Portugal); and PRACE (EU). We acknowledge the computer resources and technical assistance provided by the Spanish Supercomputing Network nodes at Universidad de Cantabria and Universidad Politécnica de Madrid as well as the support provided by the Advanced Computing and e-Science team at IFCA. A description of the Planck Collaboration and a list of its members, including the technical or scientific activ-



**Table 4.** Impact of systematic effects on skewness and kurtosis at various angular scales.

Angular scale [']	Skewness			Kurtosis		
	30 GHz	44 GHz	70 GHz	30 GHz	44 GHz	70 GHz
1.3	-0.13	-0.20	-0.06	-0.39	-0.40	-0.25
2.1	-0.09	0.09	0.58	0.08	-0.42	-0.10
3.4	-0.29	0.13	0.74	0.61	-0.04	-0.06
5.4	-2.25	-0.08	0.99	0.60	0.04	-0.88
8.7	-7.52	0.05	4.39	1.30	0.96	-6.62
13.9	-6.52	0.35	1.86	-0.20	0.75	-2.38
22.3	-1.23	-0.05	0.07	-0.79	-0.17	-0.32
35.6	-0.20	0.11	-0.12	-0.44	-0.04	-0.06
57.0	0.19	0.23	-0.21	-0.25	-0.09	-0.16
91.2	0.19	0.26	0.02	-0.02	0.25	-0.08
146.0	-0.07	0.09	0.14	-0.13	0.07	0.07
233.5	-0.06	-0.09	0.33	-1.34	0.05	-0.33
373.6	0.45	0.28	0.20	-1.56	0.08	-0.21
597.7	0.80	0.36	0.16	-0.01	0.27	-0.20
956.3	0.08	0.21	0.25	-0.05	-0.28	0.12

<sup>a</sup> Values represent the normalized difference (in %) of the mean for the skewness and the kurtosis for each scale of the SMHW, considering maps with and without systematic effects.

ities in which they have been involved, can be found at [http://www.sciops.esa.int/index.php?project=planck&page=Planck\\_Collaboration](http://www.sciops.esa.int/index.php?project=planck&page=Planck_Collaboration).

## References

- Bersanelli, M., Mandolesi, N., Butler, R. C., et al. 2010, *A&A*, 520, A4+  
 Górski, K. M., Hivon, E., Banday, A. J., et al. 2005, *ApJ*, 622, 759  
 Hinshaw, G., Weiland, J. L., Hill, R. S., et al. 2009, *ApJS*, 180, 225  
 Jarosik, N., Barnes, C., Bennett, C. L., et al. 2003, *ApJS*, 148, 29  
 Jarosik, N., Bennett, C. L., Halpern, M., et al. 2003, *The Astrophysical Journal Supplement Series*, 145, 413  
 Lamarre, J., Puget, J., Ade, P. A. R., et al. 2010, *A&A*, 520, A9+  
 Leach, S. M., Cardoso, J., Baccigalupi, C., et al. 2008, *A&A*, 491, 597  
 Leahy, J. P., Bersanelli, M., D’Arcangelo, O., et al. 2010, *A&A*, 520, A8+  
 Martínez-González, E., Gallegos, J. E., Argüeso, F., Cayón, L., & Sanz, J. L. 2002, *MNRAS*, 336, 22  
 Meinhold, P., Leonardi, R., Aja, B., et al. 2009, *Journal of Instrumentation*, 4, 2009  
 Mennella, A., Bersanelli, M., Butler, R. C., et al. 2010, *A&A*, 520, A5+  
 Mennella, A., Bersanelli, M., Seiffert, M., et al. 2003, *A&A*, 410, 1089  
 Mennella, A., Butler, R. C., Curto, A., et al. 2011, *A&A*, 536, A3  
 Planck Collaboration ES. 2013, *The Explanatory Supplement to the Planck 2013 results (ESA)*  
 Planck Collaboration I. 2013, Submitted to *A&A*  
 Planck Collaboration II. 2011, *A&A*, 536, A2  
 Planck Collaboration II. 2013, Submitted to *A&A*  
 Planck Collaboration IV. 2013, Submitted to *A&A*  
 Planck Collaboration V. 2013, Submitted to *A&A*  
 Planck Collaboration XII. 2013, Submitted to *A&A*  
 Planck Collaboration XIX. 2013, Submitted to *A&A*  
 Planck Collaboration XV. 2013, Submitted to *A&A*  
 Planck Collaboration XXIII. 2013, Submitted to *A&A*  
 Planck Collaboration XXIV. 2013, Submitted to *A&A*  
 Planck Science Office. 2010, *Science Operations “One Year” Report*, Tech. Rep. Planck/PSO/2010-75, ESA  
 Sandri, M., Villa, F., Bersanelli, M., et al. 2010, *A&A*, 520, A7+  
 Schmalzing, J. & Gorski, K. M. 1998, *MNRAS*, 297, 355  
 Seiffert, M., Mennella, A., Burigana, C., et al. 2002, *A&A*, 391, 1185

- Tauber, J. A., Norgaard-Nielsen, H. U., Ade, P. A. R., et al. 2010, *A&A*, 520, A2+  
 Terenzi, L., Salmon, M. J., Colin, A., et al. 2009, *Journal of Instrumentation*, 4, 2012  
 Tomasi, M., Cappellini, B., Gregorio, A., et al. 2010, *Journal of Instrumentation*, 5, 1002  
 Valenziano, L., Cuttaia, F., De Rosa, A., et al. 2009, *Journal of Instrumentation*, 4, 2006  
 Zacchei, A., Maino, D., Baccigalupi, C., et al. 2011, *A&A*, 536, A5  
 Zonca, A., Franceschet, C., Battaglia, P., et al. 2009, *Journal of Instrumentation*, 4, 2010

## Appendix A: Theory of the ADC non-linearity effect

The ADC non-linearity arises when the measured detector voltage differs from the true voltage in some repeatable but complicated manner, depending on the exact positions of the voltage thresholds of the chip. By finding a way to map the apparent voltage,  $V'$ , to the true voltage,  $V$ , the ADC effect can be corrected and this mapping is just the ADC response curve,  $R(V')$ , as seen through the LFI acquisition system. In a perfect radiometer this voltage is also the product of the system temperature,  $T_{\text{sys}}$ , and radiometer gain,  $G(t)$ ,

$$V = V' R(V') = G(t) T_{\text{sys}}. \quad (\text{A.1})$$

Probing the response function requires tracking how a small known input voltage variation,  $\Delta V$ , appears as a measured  $\Delta V'$  at different working voltages,  $V'$ . The way this works can be illustrated by differentiating the above equation with respect to  $V'$ , to obtain

$$\Delta V = \left( V' \frac{dR(V')}{dV'} + R(V') \right) \Delta V' = G(t) \Delta T. \quad (\text{A.2})$$

Equation (A.2) shows the relation between differential input and output signals and how a localized change in gradient can dominate via the  $dR/dV'$  term. It also shows that small intrinsic thermal noise fluctuations,  $\Delta T$ , can be used as the corresponding test input temperature signal assuming it to be due to bandwidth limited noise power  $\Delta T = T_{\text{sys}} / \sqrt{\Delta \nu \tau}$ , where  $\Delta \nu$  and  $\tau$  are channel bandwidth and sample integration time, respectively. By combining the two previous equations, the differential response can be expressed as

$$\frac{dR(V')}{dV'} = \left( \frac{1}{\sqrt{\Delta \nu \tau} \Delta V'} - \frac{1}{V'} \right) R(V'). \quad (\text{A.3})$$

In the case of no ADC effects and voltage variations induced purely through gain fluctuations, we have  $V' = \sqrt{\Delta \nu \tau} \Delta V'$ , and the differential response  $dR(V')/dV'$  remains zero for all  $V'$ , as expected. Non-linearities are signaled where the thermal white noise does not follow detector voltages, revealing variations in the response curve. Since the radiometer gains drift very slowly, many estimates of detector white noise by Fourier analysis from the one minute scan rings are available, and by binning and averaging good signal-to-noises of  $\approx 100$  are achievable. The above equation can be integrated numerically, making use of these binned values, if the factor  $R(V')$  is taken to be unity, which is a good approximation. A discrete set of corrected voltages  $V_k$  for each of the binned measured voltages  $V'_i$  can be found via a trapezoidal summation as follows:

$$V_k = V'_0 + \frac{\delta V'}{2} \sum_{i=1}^k a \left( \frac{1}{\Delta V'_{i-1}} + \frac{1}{\Delta V'_i} \right) - \left( \frac{1}{V'_{i-1}} + \frac{1}{V'_i} \right). \quad (\text{A.4})$$



Here  $V'_0$  is lowest voltage bin,  $\delta V'$  the voltage bin width, and  $a = 1/\sqrt{\Delta v \tau}$  is fitted so that the top voltage bin,  $V_{\max}$ , is equal to  $V'_{\max}$  to maintain the same overall linear response. These tables of corrected voltages to measured voltages for each detector are stored in the DPC database as the ADC correction, and are implemented as spline fits to these control points to carry out the correction on the time-ordered data.

- <sup>1</sup> APC, AstroParticule et Cosmologie, Université Paris Diderot, CNRS/IN2P3, CEA/Irfu, Observatoire de Paris, Sorbonne Paris Cité, 10, rue Alice Domon et Léonie Duquet, 75205 Paris Cedex 13, France
- <sup>2</sup> Aalto University Metsähovi Radio Observatory, Metsähovintie 114, FIN-02540 Kylmäla, Finland
- <sup>3</sup> African Institute for Mathematical Sciences, 6-8 Melrose Road, Muizenberg, Cape Town, South Africa
- <sup>4</sup> Agenzia Spaziale Italiana Science Data Center, c/o ESRIN, via Galileo Galilei, Frascati, Italy
- <sup>5</sup> Agenzia Spaziale Italiana, Viale Liegi 26, Roma, Italy
- <sup>6</sup> Astrophysics Group, Cavendish Laboratory, University of Cambridge, J J Thomson Avenue, Cambridge CB3 0HE, U.K.
- <sup>7</sup> CITA, University of Toronto, 60 St. George St., Toronto, ON M5S 3H8, Canada
- <sup>8</sup> CNRS, IRAP, 9 Av. colonel Roche, BP 44346, F-31028 Toulouse cedex 4, France
- <sup>9</sup> California Institute of Technology, Pasadena, California, U.S.A.
- <sup>10</sup> Centre for Theoretical Cosmology, DAMTP, University of Cambridge, Wilberforce Road, Cambridge CB3 0WA U.K.
- <sup>11</sup> Centro de Estudios de Física del Cosmos de Aragón (CEFCA), Plaza San Juan, 1, planta 2, E-44001, Teruel, Spain
- <sup>12</sup> Computational Cosmology Center, Lawrence Berkeley National Laboratory, Berkeley, California, U.S.A.
- <sup>13</sup> Consejo Superior de Investigaciones Científicas (CSIC), Madrid, Spain
- <sup>14</sup> DSM/Irfu/SPP, CEA-Saclay, F-91191 Gif-sur-Yvette Cedex, France
- <sup>15</sup> DTU Space, National Space Institute, Technical University of Denmark, Elektrovej 327, DK-2800 Kgs. Lyngby, Denmark
- <sup>16</sup> Département de Physique Théorique, Université de Genève, 24, Quai E. Ansermet, 1211 Genève 4, Switzerland
- <sup>17</sup> Departamento de Física Fundamental, Facultad de Ciencias, Universidad de Salamanca, 37008 Salamanca, Spain
- <sup>18</sup> Departamento de Física, Universidad de Oviedo, Avda. Calvo Sotelo s/n, Oviedo, Spain
- <sup>19</sup> Departamento de Matemáticas, Estadística y Computación, Universidad de Cantabria, Avda. de los Castros s/n, Santander, Spain
- <sup>20</sup> Department of Astronomy and Astrophysics, University of Toronto, 50 Saint George Street, Toronto, Ontario, Canada
- <sup>21</sup> Department of Astrophysics/IMAPP, Radboud University Nijmegen, P.O. Box 9010, 6500 GL Nijmegen, The Netherlands
- <sup>22</sup> Department of Electrical Engineering and Computer Sciences, University of California, Berkeley, California, U.S.A.
- <sup>23</sup> Department of Physics & Astronomy, University of British Columbia, 6224 Agricultural Road, Vancouver, British Columbia, Canada
- <sup>24</sup> Department of Physics and Astronomy, Dana and David Dornsife College of Letter, Arts and Sciences, University of Southern California, Los Angeles, CA 90089, U.S.A.
- <sup>25</sup> Department of Physics and Astronomy, University College London, London WC1E 6BT, U.K.
- <sup>26</sup> Department of Physics, Gustaf Hållströmin katu 2a, University of Helsinki, Helsinki, Finland
- <sup>27</sup> Department of Physics, Princeton University, Princeton, New Jersey, U.S.A.
- <sup>28</sup> Department of Physics, University of California, One Shields Avenue, Davis, California, U.S.A.
- <sup>29</sup> Department of Physics, University of California, Santa Barbara, California, U.S.A.
- <sup>30</sup> Department of Physics, University of Illinois at Urbana-Champaign, 1110 West Green Street, Urbana, Illinois, U.S.A.
- <sup>31</sup> Dipartimento di Fisica e Astronomia G. Galilei, Università degli Studi di Padova, via Marzolo 8, 35131 Padova, Italy
- <sup>32</sup> Dipartimento di Fisica e Scienze della Terra, Università di Ferrara, Via Saragat 1, 44122 Ferrara, Italy
- <sup>33</sup> Dipartimento di Fisica, Università La Sapienza, P. le A. Moro 2, Roma, Italy
- <sup>34</sup> Dipartimento di Fisica, Università degli Studi di Milano, Via Celoria, 16, Milano, Italy
- <sup>35</sup> Dipartimento di Fisica, Università degli Studi di Trieste, via A. Valerio 2, Trieste, Italy
- <sup>36</sup> Dipartimento di Fisica, Università di Roma Tor Vergata, Via della Ricerca Scientifica, 1, Roma, Italy
- <sup>37</sup> Discovery Center, Niels Bohr Institute, Blegdamsvej 17, Copenhagen, Denmark
- <sup>38</sup> Dpto. Astrofísica, Universidad de La Laguna (ULL), E-38206 La Laguna, Tenerife, Spain
- <sup>39</sup> European Space Agency, ESAC, Planck Science Office, Camino bajo del Castillo, s/n, Urbanización Villafranca del Castillo, Villanueva de la Cañada, Madrid, Spain
- <sup>40</sup> European Space Agency, ESTEC, Keplerlaan 1, 2201 AZ Noordwijk, The Netherlands
- <sup>41</sup> Haverford College Astronomy Department, 370 Lancaster Avenue, Haverford, Pennsylvania, U.S.A.
- <sup>42</sup> Helsinki Institute of Physics, Gustaf Hållströmin katu 2, University of Helsinki, Helsinki, Finland
- <sup>43</sup> INAF - Osservatorio Astrofisico di Catania, Via S. Sofia 78, Catania, Italy
- <sup>44</sup> INAF - Osservatorio Astronomico di Padova, Vicolo dell'Osservatorio 5, Padova, Italy
- <sup>45</sup> INAF - Osservatorio Astronomico di Roma, via di Frascati 33, Monte Porzio Catone, Italy
- <sup>46</sup> INAF - Osservatorio Astronomico di Trieste, Via G.B. Tiepolo 11, Trieste, Italy
- <sup>47</sup> INAF/IASF Bologna, Via Gobetti 101, Bologna, Italy
- <sup>48</sup> INAF/IASF Milano, Via E. Bassini 15, Milano, Italy
- <sup>49</sup> INFN, Sezione di Bologna, Via Imerio 46, I-40126, Bologna, Italy
- <sup>50</sup> INFN, Sezione di Roma 1, Università di Roma Sapienza, Piazzale Aldo Moro 2, 00185, Roma, Italy
- <sup>51</sup> IPAG: Institut de Planétologie et d'Astrophysique de Grenoble, Université Joseph Fourier, Grenoble 1 / CNRS-INSU, UMR 5274, Grenoble, F-38041, France
- <sup>52</sup> ISDC Data Centre for Astrophysics, University of Geneva, ch. d'Ecogia 16, Versoix, Switzerland
- <sup>53</sup> IUCAA, Post Bag 4, Ganeshkhind, Pune University Campus, Pune 411 007, India
- <sup>54</sup> Imperial College London, Astrophysics group, Blackett Laboratory, Prince Consort Road, London, SW7 2AZ, U.K.
- <sup>55</sup> Infrared Processing and Analysis Center, California Institute of Technology, Pasadena, CA 91125, U.S.A.
- <sup>56</sup> Institut Néel, CNRS, Université Joseph Fourier Grenoble I, 25 rue des Martyrs, Grenoble, France
- <sup>57</sup> Institut Universitaire de France, 103, bd Saint-Michel, 75005, Paris, France
- <sup>58</sup> Institut d'Astrophysique Spatiale, CNRS (UMR8617) Université Paris-Sud 11, Bâtiment 121, Orsay, France
- <sup>59</sup> Institut d'Astrophysique de Paris, CNRS (UMR7095), 98 bis Boulevard Arago, F-75014, Paris, France
- <sup>60</sup> Institute for Space Sciences, Bucharest-Magurale, Romania
- <sup>61</sup> Institute of Astronomy and Astrophysics, Academia Sinica, Taipei, Taiwan
- <sup>62</sup> Institute of Astronomy, University of Cambridge, Madingley Road, Cambridge CB3 0HA, U.K.
- <sup>63</sup> Institute of Theoretical Astrophysics, University of Oslo, Blindern, Oslo, Norway
- <sup>64</sup> Instituto de Astrofísica de Canarias, C/Vía Láctea s/n, La Laguna, Tenerife, Spain

- <sup>65</sup> Instituto de Física de Cantabria (CSIC-Universidad de Cantabria),  
Avda. de los Castros s/n, Santander, Spain
- <sup>66</sup> Istituto di Fisica del Plasma, CNR-ENEA-EURATOM Association,  
Via R. Cozzi 53, Milano, Italy
- <sup>67</sup> Jet Propulsion Laboratory, California Institute of Technology, 4800  
Oak Grove Drive, Pasadena, California, U.S.A.
- <sup>68</sup> Jodrell Bank Centre for Astrophysics, Alan Turing Building,  
School of Physics and Astronomy, The University of Manchester,  
Oxford Road, Manchester, M13 9PL, U.K.
- <sup>69</sup> Kavli Institute for Cosmology Cambridge, Madingley Road,  
Cambridge, CB3 0HA, U.K.
- <sup>70</sup> LAL, Université Paris-Sud, CNRS/IN2P3, Orsay, France
- <sup>71</sup> LERMA, CNRS, Observatoire de Paris, 61 Avenue de  
l'Observatoire, Paris, France
- <sup>72</sup> Laboratoire AIM, IRFU/Service d'Astrophysique - CEA/DSM -  
CNRS - Université Paris Diderot, Bât. 709, CEA-Saclay, F-91191  
Gif-sur-Yvette Cedex, France
- <sup>73</sup> Laboratoire Traitement et Communication de l'Information, CNRS  
(UMR 5141) and Télécom ParisTech, 46 rue Barrault F-75634  
Paris Cedex 13, France
- <sup>74</sup> Laboratoire de Physique Subatomique et de Cosmologie,  
Université Joseph Fourier Grenoble I, CNRS/IN2P3, Institut  
National Polytechnique de Grenoble, 53 rue des Martyrs, 38026  
Grenoble cedex, France
- <sup>75</sup> Laboratoire de Physique Théorique, Université Paris-Sud 11 &  
CNRS, Bâtiment 210, 91405 Orsay, France
- <sup>76</sup> Lawrence Berkeley National Laboratory, Berkeley, California,  
U.S.A.
- <sup>77</sup> Max-Planck-Institut für Astrophysik, Karl-Schwarzschild-Str. 1,  
85741 Garching, Germany
- <sup>78</sup> McGill Physics, Ernest Rutherford Physics Building, McGill  
University, 3600 rue University, Montréal, QC, H3A 2T8, Canada
- <sup>79</sup> MilliLab, VTT Technical Research Centre of Finland, Tietotie 3,  
Espoo, Finland
- <sup>80</sup> Niels Bohr Institute, Blegdamsvej 17, Copenhagen, Denmark
- <sup>81</sup> Observational Cosmology, Mail Stop 367-17, California Institute  
of Technology, Pasadena, CA, 91125, U.S.A.
- <sup>82</sup> SB-ITP-LPPC, EPFL, CH-1015, Lausanne, Switzerland
- <sup>83</sup> SISSA, Astrophysics Sector, via Bonomea 265, 34136, Trieste,  
Italy
- <sup>84</sup> School of Physics and Astronomy, Cardiff University, Queens  
Buildings, The Parade, Cardiff, CF24 3AA, U.K.
- <sup>85</sup> School of Physics and Astronomy, University of Nottingham,  
Nottingham NG7 2RD, U.K.
- <sup>86</sup> Space Sciences Laboratory, University of California, Berkeley,  
California, U.S.A.
- <sup>87</sup> Special Astrophysical Observatory, Russian Academy of Sciences,  
Nizhnij Arkhyz, Zelenchukskiy region, Karachai-Cherkessian  
Republic, 369167, Russia
- <sup>88</sup> Stanford University, Dept of Physics, Varian Physics Bldg, 382 Via  
Pueblo Mall, Stanford, California, U.S.A.
- <sup>89</sup> Sub-Department of Astrophysics, University of Oxford, Keble  
Road, Oxford OX1 3RH, U.K.
- <sup>90</sup> Theory Division, PH-TH, CERN, CH-1211, Geneva 23,  
Switzerland
- <sup>91</sup> UPMC Univ Paris 06, UMR7095, 98 bis Boulevard Arago,  
F-75014, Paris, France
- <sup>92</sup> Université de Toulouse, UPS-OMP, IRAP, F-31028 Toulouse cedex  
4, France
- <sup>93</sup> University of Granada, Departamento de Física Teórica y del  
Cosmos, Facultad de Ciencias, Granada, Spain
- <sup>94</sup> University of Miami, Knight Physics Building, 1320 Campo Sano  
Dr., Coral Gables, Florida, U.S.A.
- <sup>95</sup> Warsaw University Observatory, Aleje Ujazdowskie 4, 00-478  
Warszawa, Poland